

CERN-EP-2022-021
2022/05/10

CMS-HIG-20-007

Constraints on anomalous Higgs boson couplings to vector bosons and fermions from the production of Higgs bosons using the $\tau\tau$ final state

The CMS Collaboration

Abstract

A study of anomalous couplings of the Higgs boson to vector bosons and fermions is presented. The data were recorded by the CMS experiment at a center-of-mass energy of pp collisions at the LHC of 13 TeV and correspond to an integrated luminosity of 138 fb^{-1} . The study uses Higgs boson candidates produced mainly in gluon fusion or electroweak vector boson fusion at the LHC that subsequently decay to a pair of τ leptons. Matrix-element and machine-learning techniques were employed in a search for anomalous interactions. The results are combined with those from the four-lepton and two-photon decay channels to yield the most stringent constraints on anomalous Higgs boson couplings to date. The pure CP -odd scenario of the Higgs boson coupling to gluons is excluded at 2.4 standard deviations. The results are consistent with the standard model predictions.

Submitted to Physical Review D

1 Introduction

The discovery of the Higgs boson (H) by the ATLAS and CMS experiments at the LHC [1–3] has opened a new era for particle physics, wherein the characterization of the new boson is of crucial importance. Studies of the Higgs boson test the standard model (SM) of particle physics and probe for new physics. Thus far, the properties of the H are found to be consistent with the SM predictions [4–10]. In particular, nonzero spin assignments of the H have been excluded [11, 12], and its spin-parity quantum numbers are consistent with $J^{PC} = 0^{++}$ [11–31]. However, the limited precision of current studies allows for anomalous couplings of the H with two electroweak gauge bosons (HVV) or gluons (Hgg). Possible CP -violating effects in H couplings to fermions (Hff) have been constrained by the CMS and ATLAS Collaborations in $t\bar{t}H$ production [20, 21, 30], and by the CMS Collaboration in the $H \rightarrow \tau\tau$ decay [22], where CP -odd couplings may appear at tree level, and are not suppressed by loop effects. In the SM, Hgg is mediated via loops, where the top quark dominates. Any observed CP violation in the Hgg interaction would indicate either a CP -odd Higgs coupling to top quarks (Htt) or a new effective interaction requiring new particles. Thus, a study of the Hgg coupling provides complementary information on the nature of the H and serves as an indirect search for new phenomena. Both the CMS and ATLAS Collaborations have previously searched for CP -violation in the Hgg coupling, but these constraints are quite weak [21, 31].

In this paper, we report on a search for anomalous effects, including possible signs of CP violation, in the tensor structure of the H interactions with electroweak bosons and gluons in the production of the H. The analysis is performed in four $\tau\tau$ final states: $e\mu$, $e\tau_h$, $\mu\tau_h$, and $\tau_h\tau_h$, where e , μ and τ_h indicate τ decays into electrons, muons and hadrons, respectively. We follow the formalism used in previous CMS studies of anomalous couplings in Run 1 and Run 2, described in Refs. [11, 14–21]. The two dominant production channels employed in this study are electroweak vector boson fusion (VBF) and gluon fusion (ggH). Compared to our previous study in the $H \rightarrow \tau\tau$ channel [19], we have improved the sensitivity to anomalous effects with multivariate tools, optimization of the final state categorization, and an increased data sample. The analysis utilizes a matrix element likelihood approach (MELA) [13, 32–35] and a neural network to optimize the measurement of anomalous couplings using production and decay kinematic information. Compared to our similar study in the $H \rightarrow 4\ell$ channel [21], where ℓ denotes an electron or muon and both production and decay information is used, the inclusion of the $H \rightarrow \tau\tau$ channel leads to a substantial improvement in constraints on anomalous couplings due to a larger sample of VBF and ggH events reconstructed in association with two jets. The results obtained from the two decay channels are further combined to form the most stringent constraint on anomalous couplings. The combined ggH results are further combined with the $t\bar{t}H$ analysis using the $H \rightarrow \gamma\gamma$ and $H \rightarrow 4\ell$ decays [20, 21] under the assumption of top quark dominance in ggH to constrain the Htt anomalous couplings.

The paper is organized as follows. The phenomenology of anomalous HVV and Hff couplings is discussed in Section 2. The kinematics of the processes studied and the observables utilized in this study to search for anomalous contributions are described in Section 3. The data used in this study, the Monte Carlo (MC) simulation, as well as event reconstruction methods are described in Section 4. The event selection and categorization is documented in Section 6. Methods to estimate backgrounds are given in Section 7 and the sources of systematic uncertainty are listed in Section 8. The analyses of the Hgg and HVV interactions using $H \rightarrow \tau\tau$ decays are presented in Sections 9 and 10, respectively. The combination of the $H \rightarrow \tau\tau$ results with the $H \rightarrow 4\ell$ and $H \rightarrow \gamma\gamma$ decay channels is detailed in Section 11. Section 12 summarizes the results. Tabulated results are provided in the HEPData record for this analysis [36].

2 Phenomenology of anomalous couplings and cross sections

In this study, we follow the formalism used in the measurement of H couplings in earlier CMS analyses [11, 14–21]. The theoretical approach is described in Refs. [32–35, 37–45].

Interactions of a spin-0 H with two spin-1 gauge bosons VV, such as WW, ZZ, Zγ, γγ, and gg, are parameterized by a scattering amplitude that includes three tensor structures with expansion of coefficients up to (q^2/Λ_1^2) :

$$\mathcal{A}(\text{HVV}) \sim \left[a_1^{\text{VV}} + \frac{\kappa_1^{\text{VV}} q_1^2 + \kappa_2^{\text{VV}} q_2^2}{(\Lambda_1^{\text{VV}})^2} \right] m_{V1}^2 \epsilon_{V1}^* \epsilon_{V2}^* + a_2^{\text{VV}} f_{\mu\nu}^{*(1)} f^{*(2)\mu\nu} + a_3^{\text{VV}} f_{\mu\nu}^{*(1)} \tilde{f}^{*(2)\mu\nu}, \quad (1)$$

where q_i , ϵ_{Vi} , and m_{V1} are the four-momentum, polarization vector, and pole mass of the gauge boson, indexed by $i = 1, 2$. The gauge boson's field strength tensor and the dual field strength tensor are $f^{(i)\mu\nu} = \epsilon_{\nu i}^\mu q_i^\nu - \epsilon_{\nu i}^\nu q_i^\mu$ and $\tilde{f}_{\mu\nu}^{(i)} = \frac{1}{2} \epsilon_{\mu\nu\rho\sigma} f^{(i)\rho\sigma}$. The coupling coefficients a_i^{VV} , which multiply the three tensor structures, and $\kappa_i^{\text{VV}}/(\Lambda_1^{\text{VV}})^2$, which multiply the next term in the q^2 expansion for the first tensor structure, are to be determined from data, where Λ_1 is the scale of beyond the SM (BSM) physics. The convention $\epsilon_{0123} = +1$ defines the relative sign of the CP-odd and CP-even couplings. The sign in front of the gauge fields in the covariant derivative defines the sign of the photon field and sets the sign convention of the Zγ couplings. The conventions adopted in this analysis are discussed in Section 5.

In Eq. (1), the only nonzero SM contributions at tree level are a_1^{WW} and a_1^{ZZ} , which are assumed to be equal under custodial symmetry. All other ZZ and WW couplings are considered anomalous contributions, which are either due to BSM physics or small contributions arising in the SM from loop effects that cannot be detected with the current precision [46]. Among the anomalous contributions, considerations of symmetry and gauge invariance require $a_1^{\text{Z}\gamma} = a_1^{\gamma\gamma} = a_1^{\text{gg}} = 0$, $\kappa_1^{\text{ZZ}} = \kappa_2^{\text{ZZ}}$, $\kappa_1^{\gamma\gamma} = \kappa_2^{\gamma\gamma} = 0$, $\kappa_1^{\text{gg}} = \kappa_2^{\text{gg}} = 0$, and $\kappa_1^{\text{Z}\gamma} = 0$ [47]. For the gg couplings, the only nonzero couplings are a_2^{gg} and a_3^{gg} , which are anomalous contributions due to BSM physics and do not account for interactions mediated by SM particles via loops. Therefore, in total there are 13 independent parameters that describe the H coupling to the electroweak gauge bosons and two that describe the coupling to gluons. The a_3^{VV} couplings are CP-odd, and their presence together with any other CP-even couplings would result in CP violation in a given process.

Our earlier measurements [11] and a more recent phenomenological study [46] indicated substantially stronger limits on $a_2^{\gamma\gamma, \text{Z}\gamma}$ and $a_3^{\gamma\gamma, \text{Z}\gamma}$ couplings from $\text{H} \rightarrow \text{Z}\gamma$ and $\text{H} \rightarrow \gamma\gamma$ decays with on-shell photons than from measurements with virtual photons, so we do not pursue measurements of these parameters in this paper, and they are set to zero when measuring other anomalous couplings.

As the event kinematics of the H production in WW fusion and in ZZ fusion are very similar, it is essentially impossible to distinguish between a_i^{WW} and a_i^{ZZ} in the VBF production. It is therefore necessary to choose a convention to set the relative size of the HWW and HZZ couplings. The results can be reinterpreted for any chosen relationship between the a_i^{WW} and a_i^{ZZ} couplings [18].

In our measurements, we adopt two approaches to set the relationship between the a_i^{WW} and a_i^{ZZ} couplings. In the first approach (Approach 1) they are analyzed together assuming $a_i^{\text{WW}} = a_i^{\text{ZZ}}$ and $\kappa_i^{\text{ZZ}}/(\Lambda_1^{\text{ZZ}})^2 = \kappa_i^{\text{WW}}/(\Lambda_1^{\text{WW}})^2$. In the second approach (Approach 2) we reinterpret the results for the CP-violating coupling a_3 following the procedure described in Ref. [18].

In this reinterpretation we apply additional considerations of custodial and $SU(2) \times U(1)$ symmetries in the relationships of anomalous couplings [47, 48]. With $a_3^{\gamma\gamma}$ and $a_3^{Z\gamma}$ set to zero, we are left with a simple relationship between a_3^{WW} and a_3^{ZZ} ,

$$a_3^{WW} = \cos^2 \theta_W a_3^{ZZ}. \quad (2)$$

It is convenient to measure the effective cross section ratios f_{ai} rather than the anomalous couplings a_i themselves, as most uncertainties cancel in the ratio. Moreover, the effective fractions are conveniently bounded between -1 and 1 , independent of the coupling convention. The effective fractional cross sections f_{ai} are defined as follows [21]:

$$\begin{aligned} f_{a3} &= \frac{|a_3|^2 \sigma_3}{|a_1|^2 \sigma_1 + |a_2|^2 \sigma_2 + |a_3|^2 \sigma_3 + |\kappa_1|^2 \sigma_{\Lambda 1} + |\kappa_1^{Z\gamma}|^2 \sigma_{\Lambda 1}^{Z\gamma}} \operatorname{sgn} \left(\frac{a_3}{a_1} \right), \\ f_{a2} &= \frac{|a_2|^2 \sigma_2}{|a_1|^2 \sigma_1 + |a_2|^2 \sigma_2 + |a_3|^2 \sigma_3 + |\kappa_1|^2 \sigma_{\Lambda 1} + |\kappa_1^{Z\gamma}|^2 \sigma_{\Lambda 1}^{Z\gamma}} \operatorname{sgn} \left(\frac{a_2}{a_1} \right), \\ f_{\Lambda 1} &= \frac{|\kappa_1|^2 \sigma_{\Lambda 1}}{|a_1|^2 \sigma_1 + |a_2|^2 \sigma_2 + |a_3|^2 \sigma_3 + |\kappa_1|^2 \sigma_{\Lambda 1} + |\kappa_1^{Z\gamma}|^2 \sigma_{\Lambda 1}^{Z\gamma}} \operatorname{sgn} \left(\frac{-\kappa_1}{a_1} \right), \\ f_{\Lambda 1}^{Z\gamma} &= \frac{|\kappa_2^{Z\gamma}|^2 \sigma_{\Lambda 1}^{Z\gamma}}{|a_1|^2 \sigma_1 + |a_2|^2 \sigma_2 + |a_3|^2 \sigma_3 + |\kappa_1|^2 \sigma_{\Lambda 1} + |\kappa_1^{Z\gamma}|^2 \sigma_{\Lambda 1}^{Z\gamma}} \operatorname{sgn} \left(\frac{-\kappa_2^{Z\gamma}}{a_1} \right), \end{aligned} \quad (3)$$

where σ_i is the cross section for the process corresponding to $a_i = 1$ with all other couplings set to zero. The choice of the sign for the κ_1 and $\kappa_2^{Z\gamma}$ terms follows the convention introduced in the prior results [11, 17, 18, 21]. The other sign conventions follow the JHUGEN 7.0.2 [32–35] event generator, as discussed in Section 5 and Ref. [46]. For consistency with previous CMS measurements in the $H \rightarrow 4\ell$ channel [11, 21], the σ_i coefficients are defined for the $gg \rightarrow H \rightarrow VV \rightarrow 2e2\mu$ process. The numerical values are given in Table 1 as calculated using the JHUGEN event generator. It is assumed that the couplings in Eq. (1) are constant and real, and therefore this formulation is equivalent to an effective Lagrangian formalism.

Table 1: Cross sections for the anomalous contributions (σ_i) used to define the fractional cross sections [21]. The σ_i values are defined as the cross section computed with $a_i = 1$ and all other couplings set to zero. All cross sections are given relative to the SM value (σ_1). In the case of the κ_1 and $\kappa_2^{Z\gamma}$ couplings, the numerical values $\Lambda_1 = \Lambda_1^{Z\gamma} = 100 \text{ GeV}$ are considered so as to keep all coefficients of similar order of magnitude.

Coupling	σ_i/σ_1
a_3	0.153
a_2	0.361
κ_1	0.682
$\kappa_2^{Z\gamma}$	1.746

The ggH process is a purely loop-induced process, which in the SM is generated by the top quark, with a smaller contribution from the bottom quark [49]. This interaction is CP -even in the SM. However, a contribution of the CP -odd interaction in the H coupling to fermions is not ruled out, and the search for such a CP -violating interaction can be performed in $t\bar{t}H$ production and $H \rightarrow \tau\tau$ decay. Under the assumption that other BSM particles do not contribute to the gluon fusion loop, a CP -structure measurement in the ggH process is equivalent to the

measurement of the CP structure in Yukawa interactions, which can be parameterized with the amplitude

$$\mathcal{A}(\text{Hff}) = -\frac{m_f}{v} \bar{\psi}_f \left(\kappa_f + i \tilde{\kappa}_f \gamma_5 \right) \psi_f. \quad (4)$$

The effective fractional cross section for Hff couplings is defined as [20]

$$f_{CP}^{\text{Hff}} = \frac{|\tilde{\kappa}_f|^2}{|\kappa_f|^2 + |\tilde{\kappa}_f|^2} \text{sgn} \left(\frac{\tilde{\kappa}_f}{\kappa_f} \right). \quad (5)$$

An equivalent effective mixing angle α^{Hff} is also used to describe the CP -odd contribution to the H Yukawa couplings and is defined as

$$\alpha^{\text{Hff}} = \tan^{-1} \left(\frac{\tilde{\kappa}_f}{\kappa_f} \right), \quad (6)$$

where $|f_{CP}^{\text{Hff}}| = \sin^2 \alpha^{\text{Hff}}$. Therefore, with just two contributions to the gluon fusion loop (CP -even and CP -odd fermion couplings), the two parameters are equivalent. However, with consideration of multiple contributions, as discussed in the case of electroweak HVV couplings above, multiple fractional contributions have to be defined and a single angle is not sufficient. The ggH loop can be generated by unknown heavy BSM particles, in addition to the SM fermions, and the effective coupling results in the CP -even a_2^{gg} and CP -odd a_3^{gg} couplings, defined in Eq. (1). In the effective field theory (EFT) approach [48], they correspond to two EFT couplings in the Higgs basis:

$$\begin{aligned} c_{\text{gg}} &= -\frac{1}{2\pi\alpha_S} a_2^{\text{gg}}, \\ \tilde{c}_{\text{gg}} &= -\frac{1}{2\pi\alpha_S} a_3^{\text{gg}}, \end{aligned} \quad (7)$$

where α_S is the running strong coupling constant. Therefore, there are at least four contributions to consider $(\kappa_t, \tilde{\kappa}_t, c_{\text{gg}}, \tilde{c}_{\text{gg}})$, where in the SM we have $(\kappa_t, \tilde{\kappa}_t, c_{\text{gg}}, \tilde{c}_{\text{gg}}) = (1, 0, 0, 0)$. The dependence of the ggH cross section and H branching fractions on these parameters is given in Ref. [46]. Under the assumptions that the only SM particles contributing to the loop are the top and bottom quarks and $(\kappa_b, \tilde{\kappa}_b) = (1, 0)$, the ggH cross section relative to the SM expectation is given as

$$\begin{aligned} \mu_{\text{ggH}} &= 1.1068\kappa_t^2 + 0.0082 - 0.1150\kappa_t + 2.5717\tilde{\kappa}_t^2 + 1.0298(12\pi^2 c_{\text{gg}})^2 + 2.3170(8\pi^2 \tilde{c}_{\text{gg}})^2 \\ &\quad + 2.1357(12\pi^2 c_{\text{gg}})\kappa_t - 0.1109(12\pi^2 c_{\text{gg}}) + 4.8821(8\pi^2 \tilde{c}_{\text{gg}})\tilde{\kappa}_t. \end{aligned} \quad (8)$$

Within the framework of our analysis, however, it is hard to distinguish between the κ_f and a_2^{gg} contributions, or between $\tilde{\kappa}_f$ and a_3^{gg} . There are small differences in the transverse momentum p_T distributions of the H, and one can also observe effects in the off-shell H production [47]. However, the former is too small to have a noticeable effect in this analysis, and the latter does not come within the scope of our analysis based on the on-shell production. Therefore, we absorb the SM fermion loop contribution, dominated by the heavy top quark, into the overall a_2^{gg} and a_3^{gg} couplings. The only remaining effective fractional cross section for the Hgg interaction is defined as [21]

$$f_{a3}^{\text{ggH}} = \frac{|a_3^{\text{gg}}|^2}{|a_2^{\text{gg}}|^2 + |a_3^{\text{gg}}|^2} \text{sgn} \left(\frac{a_3^{\text{gg}}}{a_2^{\text{gg}}} \right). \quad (9)$$

Under the assumption that only the top and bottom quarks contribute to gluon fusion with $\kappa_t = \kappa_b$ and $\tilde{\kappa}_t = \tilde{\kappa}_b$, the following relationship [47] holds:

$$|f_{CP}^{H\tau\tau}| = \left(1 + 2.38 \left[\frac{1}{|f_{a3}^{ggH}|} - 1 \right] \right)^{-1}. \quad (10)$$

In this paper, we present a search for anomalous Hgg couplings in the gluon fusion production and anomalous HVV couplings in VBF and associative H production with a W or Z boson (VH). In addition, the Hgg measurement is interpreted in terms of constraints on Hff couplings under the assumption of top quark dominance in gluon fusion. We measure a given anomalous coupling while setting the values of all other anomalous coupling parameters to zero, with the exception of measuring the CP -odd parameters, f_{a3} and f_{a3}^{ggH} , as CP violation in VBF and VH production would modify the same kinematic distributions as those in the ggH process. Therefore, we treat f_{a3} as an unconstrained parameter when we measure f_{a3}^{ggH} , and vice versa. The presence of CP violation in the decay of the H to a pair of τ leptons does not affect the measurements of the production process, and thus we assume the SM kinematics for the H decays.

3 Production and decay kinematics, and discriminants

Because exotic nonzero spin assignments of the H have been excluded [11–31], we focus on the analysis of couplings of a spin-0 H. When combined with the momentum transfer of the vector bosons, the five angles illustrated in Fig. 1 provide complete kinematic information for production and decay of the H.

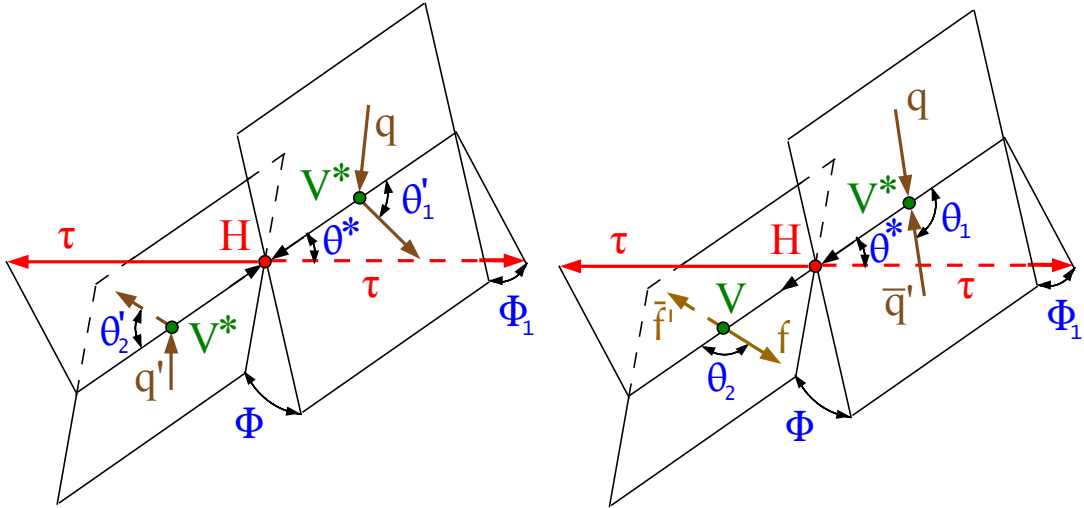


Figure 1: Illustrations of H production in VBF ($qq' \rightarrow qq'H$) (left) and VH ($qq' \rightarrow V^* \rightarrow VH \rightarrow qq'H$) (right) in the rest frame of the H. The decay $H \rightarrow \tau\tau$ is shown without illustrating the further decay chain. The incoming partons and fermions in the V decay are shown in brown and the intermediate or final-state particles are shown in red and green. The angles characterizing kinematic distributions are shown in blue and are defined in the respective rest frames [32, 34]. The illustration for H production via ggH in association with two jets is identical to the VBF diagram, except with $V = g$.

There are four possible and practical ways to access CP -violating effects (or more generally anomalous HVV or Hff couplings) using the reconstructed $H \rightarrow \tau\tau$ events:

1. correlation of H and two quark jets or leptons in VBF and VH production;
2. correlation of H and two quark jets in ggH production;
3. correlation of H and quark jets in $t\bar{t}H$ or tH production; and
4. correlation of decay products of two τ leptons.

There are no spin correlations between the production and decay through a spin-0 object. Therefore, all four of the above processes can be studied independently and they target different parameters that are independent, even though all of them may be related to anomalous effects. This analysis focuses on searching for anomalous effects in the topologies described as the first and second items above. We refer to those as the anomalous HVV and Hgg couplings, respectively.

3.1 Correlation of H and two quark jets or leptons in VBF and VH production

Kinematic distributions of associated particles in VBF and VH production are sensitive to the quantum numbers and anomalous couplings of the H . A set of observables could be defined in production, such as $\Omega^{\text{assoc}} = \{\theta_1^{\text{VBF}}, \theta_2^{\text{VBF}}, \theta^{*\text{VBF}}, \Phi^{\text{VBF}}, \Phi_1^{\text{VBF}}, q_1^{2,\text{VBF}}, q_2^{2,\text{VBF}}\}$ for the VBF process or $\Omega^{\text{assoc}} = \{\theta_1^{\text{VH}}, \theta_2^{\text{VH}}, \theta^{*\text{VH}}, \Phi^{\text{VH}}, \Phi_1^{\text{VH}}, q_1^{2,\text{VH}}, q_2^{2,\text{VH}}\}$ for the VH process (as shown in Fig. 1 and discussed in Ref. [34]). It is a challenging task to perform an optimal analysis in a multi-dimensional space of observables. The MELA method introduced earlier [2, 32–35] is designed to reduce the number of observables to the minimum, while retaining all essential information. Two types of discriminants are defined for the production process. One type of discriminant separates the process with anomalous couplings (denoted as generic BSM here) from the SM one:

$$\mathcal{D}_{\text{BSM}} = \frac{\mathcal{P}_{\text{SM}}(\vec{\Omega})}{\mathcal{P}_{\text{SM}}(\vec{\Omega}) + \mathcal{P}_{\text{BSM}}(\vec{\Omega})}, \quad (11)$$

where the probability density \mathcal{P} of a certain process (either SM or anomalous signal) is calculated using the MELA [32–35] package, that contains a library of matrix elements for the signal processes from JHUGEN. The discriminant for each anomalous coupling is listed in Table 2.

Table 2: List of discriminants for separating anomalous couplings from the SM contribution.

Coupling	Discriminant
a_3^{gg}	$\mathcal{D}_{0-}^{\text{ggH}}$
a_3	\mathcal{D}_{0-}
a_2	\mathcal{D}_{0h+}
κ_1	$\mathcal{D}_{\Lambda 1}$
$\kappa_2^{Z\gamma}$	$\mathcal{D}_{\Lambda 1}^{Z\gamma}$

The second type of discriminant isolates the interference contribution:

$$\mathcal{D}_{\text{int}} = \frac{\mathcal{P}_{\text{SM-BSM}}^{\text{int}}(\vec{\Omega})}{\mathcal{P}_{\text{SM}}(\vec{\Omega}) + \mathcal{P}_{\text{BSM}}(\vec{\Omega})}, \quad (12)$$

where $\mathcal{P}_{\text{SM-BSM}}^{\text{int}}$ is the interference part of the probability distribution for a process with a mixture of the SM and anomalous contributions. This discriminant is called $\mathcal{D}_{\text{CP}}^{\text{VBF}} (\mathcal{D}_{\text{CP}}^{\text{ggH}})$ in the CP -odd VBF (ggH) amplitude analysis. The discriminant in this case is a CP -odd observable, and a forward-backward asymmetry in its distribution would indicate CP violation. Probabilities are normalized for the matrix elements to give the same cross sections in the relevant phase space of each process. Such normalization leads to a balanced distribution of events in the range between 0 and 1, or between -1 and 1, for the \mathcal{D}_{BSM} and \mathcal{D}_{int} discriminants, respectively.

The two other observables in Eqs. (11) and (12) rely only on signal matrix elements and are well-defined. One can apply the Neyman–Pearson lemma to prove that, in the absence of detector smearing, they become the minimal and complete set of optimal observables [34, 35] for the measurement of the f_{ai} parameters defined in Section 2.

In application to the CP measurement with the f_{a3} parameter, the two optimal observables are called \mathcal{D}_{0-} and $\mathcal{D}_{\text{CP}}^{\text{VBF}}$, because $J^P = 0^-$ is the BSM hypothesis in this case, and the interference discriminant is an unambiguously CP -sensitive observable. A distinct forward-backward asymmetry in the $\mathcal{D}_{\text{CP}}^{\text{VBF}}$ distribution (forward defined as $\mathcal{D}_{\text{CP}}^{\text{VBF}} > 0$ and backward as $\mathcal{D}_{\text{CP}}^{\text{VBF}} < 0$) appears only in the presence of CP violation. These observables could be defined for both VBF and VH processes. However, since the analysis selection is optimized for the VBF process, the probabilities in the discriminant calculation in Eqs. (11) and (12) are defined for the VBF process.

3.2 Correlation of H and two jets in the production of H via ggH

Kinematic distributions of associated particles in ggH production are also sensitive to the quantum numbers and anomalous Hgg couplings. The set of observables Ω in this topology is identical to the VBF process (as shown in Fig. 1 and discussed in Ref. [34]).

Similar to the VBF and VH study, we form optimal $\mathcal{D}_{0-}^{\text{ggH}}$ and $\mathcal{D}_{\text{CP}}^{\text{ggH}}$ observables that are sensitive to CP violation. However, unlike in the VBF production study, the sensitivity to CP violation using MELA observables in ggH production is comparable to the signed azimuthal difference between two leading jets, defined as [50]

$$\Delta\phi_{jj} = \phi(j_1) - \phi(j_2), \text{ with } \eta(j_1) < \eta(j_2). \quad (13)$$

The sign is defined by ordering the jets in η , which ensures that the observable is sensitive to the interference between the CP -even and CP -odd contributions [37, 38, 51]. Thus, in this study we cross check the results obtained using the MELA discriminants with a simplified approach that does not rely on multivariate techniques and utilizes $\Delta\phi_{jj}$ as the CP -sensitive observable. We will refer to these approaches as the “MELA method” and the “ $\Delta\phi_{jj}$ method”, respectively.

4 The CMS detector

The main feature of the CMS detector is a superconducting solenoid of 6 m internal diameter, that provides a magnetic field of 3.8 T. Within the volume of the solenoid, there are a silicon pixel and strip tracker detectors, as well as a lead tungstate crystal electromagnetic calorimeter

(ECAL), and a brass and scintillator hadron calorimeter; both calorimeters are composed of a barrel and two endcap sections. Forward calorimeters extend the coverage in pseudorapidity, η . The CMS muon system is comprised of gas-ionization chambers embedded in the steel flux-return yoke outside the CMS solenoid.

The CMS data acquisition system employs a two-tiered trigger system [52] to select events of interest. The first level (L1), composed of custom hardware processors, utilizes information from muon detectors and both calorimeters to select collision events at a rate of about 100 kHz within a fixed latency below $4 \mu\text{s}$. The second level, also known as the high-level trigger, further reduces the event acceptance rate to about 1 kHz before data storage by using a full event reconstruction software, optimized for fast processing, running on a computing farm.

A more detailed description of the CMS detector, together with a definition of the coordinate system used and the relevant kinematic variables, can be found in Ref. [53].

5 Data and simulation samples

The data samples used in this analysis correspond to integrated luminosities of 36.3, 41.5 and 59.7 fb^{-1} collected in 2016, 2017 and 2018, respectively, for a total of 138 fb^{-1} collected during Run 2 of the CERN LHC at a proton-proton (pp) center-of-mass collision energy of 13 TeV [54–56].

MC simulation is used to model signal and background processes in pp interactions at the LHC and their reconstruction in the CMS detector. All MC samples are interfaced with the PYTHIA [57] generator for parton showering, where versions 8.212 and 8.226 are used for 2016, and version 8.230 is used for 2017–2018 simulations. All the MC samples are further processed through a dedicated CMS detector simulation based on the GEANT4 program [58].

Following the formalism discussed in Section 2, the samples with the SM and anomalous H couplings in VBF and VH production are generated with the JHUGEN program at leading order (LO) in quantum chromodynamics (QCD). All the simulated scenarios are reweighted to model any other set of H couplings using the MELA package. The VBF and VH JHUGEN SM simulations, after parton showering modeling, are explicitly compared with the next-to-leading order (NLO) QCD SM simulations produced by POWHEG 2.0 [59–64] and no significant differences are found in kinematic observables. Therefore, the JHUGEN simulation is used to describe kinematics of the VBF and VH processes with anomalous coupling effects in VBF and VH processes, with the expected yields scaled to match the SM theoretical predictions for inclusive cross sections and $H \rightarrow \tau\tau$ branching fraction from Ref. [48], and the POWHEG 2.0 SM prediction of relative event yields in the categorization of events based on associated particles.

Anomalous ggH events are produced with up to two jets at NLO QCD accuracy using MADGRAPH5_aMC@NLO 2.6.0 [65–67] and are also studied with JHUGEN at LO. The inclusive cross section and $H \rightarrow \tau\tau$ branching fraction are scaled to match the SM theoretical predictions from Ref. [48], and the p_T and jet multiplicity distributions are reweighted to match the POWHEG NNLOPS predictions [49, 68]. The relationship between the Hff and Hgg couplings follows JHUGEN with the relative sign of CP -odd and CP -even coefficients opposite to that assumed in MADGRAPH5_aMC@NLO 2.6.0. This choice corresponds to the convention $\epsilon_{0123} = +1$ [47]. The sign convention of the photon field in JHUGEN is opposite to that in MADGRAPH5_aMC@NLO, which leads to the opposite sign of the $HZ\gamma$ couplings. This sign convention depends on the sign in front of the gauge fields in the covariant derivative and this analysis follows $D_\mu = \partial_\mu - ie\sigma^i W_\mu^i / (2s_w) + ieB_\mu / (2c_w)$ used in JHUGEN [46].

The PYTHIA event generator is used to model the H decay to τ leptons and the decays of the τ leptons. Both scalar and pseudoscalar $H \rightarrow \tau\tau$ decays and their interference have been simulated to confirm that the observables used in the analysis are not sensitive to anomalous couplings affecting the $H \rightarrow \tau\tau$ decays. Thus, the default samples are generated with the SM $H \rightarrow \tau\tau$ decay process.

The MADGRAPH5_aMC@NLO [65] generator is used to produce W +jets and $Z \rightarrow ee/\mu\mu$ +jets samples at LO accuracy. The MADGRAPH5_aMC@NLO generator is also used for diboson production simulated at NLO, whereas POWHEG version 2.0 is used for $t\bar{t}$ [69] and single top quark (t -channel) production [70], and POWHEG version 1.0 is used for single top quark production in association with a W boson [71].

For processes simulated at NLO (LO) in QCD with the MADGRAPH5_aMC@NLO generator, events characterized by different parton multiplicities from the matrix element calculation are merged via the FxFx [66] (MLM [72]) prescription.

The PYTHIA parameters affecting the description of the underlying event are set to the CUETP8M1 [73] tune for 2016 simulations, except for the $t\bar{t}$ sample where the CUETP8M2T4 [74] tune is used, and the CP5 [75] tune for 2017–2018 simulations. We use the NNPDF 3.0 [76] (3.1 [77]) parton distribution functions, PDFs, for 2016 (2017–2018) simulations.

Simulated events include the contribution from additional pp interactions within the same or adjacent bunch crossings (pileup) and are weighted to reproduce the observed pileup distribution in data.

6 Event selection

The reconstruction of recorded and simulated events relies on the particle-flow (PF) algorithm [78], which combines the information from the CMS subdetectors to identify and reconstruct muons, electrons, photons, and charged and neutral hadrons emerging from pp collisions. Combinations of these PF candidates are used to reconstruct higher-level objects such as jets, τ candidates, or missing transverse momentum, \vec{p}_T^{miss} .

The primary vertex (PV) is taken to be the vertex corresponding to the hardest scattering in the event, evaluated using tracking information alone, as described in Section 9.4.1 of Ref. [79].

Electrons are identified with a multivariate discriminant combining several quantities describing the track quality, the shape of the energy deposits in the ECAL, and the compatibility of the measurements from the tracker and the ECAL [80]. Muons are identified with requirements on the quality of the track reconstruction and on the number of measurements in the tracker and the muon systems [81]. A relative isolation variable, I^ℓ , is defined as the total energy deposited in a cone of size of $R < 0.3$ (0.4) centered on the electron (muon) direction divided by the p_T of the lepton. The expected contribution to the energy sum from pileup interactions is estimated and subtracted from the total. To reject lepton candidates arising from misidentified jet constituents or from hadron decays, we require that $I^\ell < 0.15$.

Hadronic jets are clustered from the reconstructed PF particles using the infrared and collinear safe anti- k_T algorithm [82, 83] with a distance parameter $\Delta R = \sqrt{(\Delta\eta)^2 + (\Delta\phi)^2}$ of 0.4. Jet momentum is determined as the vector sum of all particle momenta in the jet, and is found from simulation to be, on average, within 5 to 10% of the true momentum over the whole p_T spectrum and detector acceptance. Pileup interactions can contribute additional tracks and calorimetric energy depositions to the jet momentum. To mitigate this effect, charged parti-

cles identified to be originating from pileup vertices are discarded and an offset correction is applied to correct for the remaining contributions. Jet energy corrections are derived from simulation to bring the measured response of jets to that of particle level jets on average. In situ measurements of the momentum balance in dijet, photon + jet, Z + jet, and multijet events are used to account for any residual differences in the jet energy scale between data and simulation [84]. The jet energy resolution amounts typically to 15–20% at 30 GeV, 10% at 100 GeV, and 5% at 1 TeV [84]. Additional selection criteria are applied to each jet to remove jets potentially dominated by anomalous contributions from various subdetector components or reconstruction failures. In this analysis, jets are required to have $p_T > 30$ GeV and $|\eta| < 4.7$, and to be separated from the reconstructed visible τ decay products by a distance parameter of at least 0.5, where ϕ is the azimuthal angle in radians. Data collected in the most forward region of the ECAL endcaps were affected by large amounts of noise during the 2017 run, which led to disagreements between simulation and data. To mitigate this effect, jets used in the analysis of the 2017 data are discarded if they have $p_T < 50$ GeV and $2.650 < |\eta| < 3.139$. Hadronic jets that contain b quarks (“b jets”) are identified using a deep neural network (DNN), called the Deep Combined Secondary Vertex algorithm [85].

Hadronically decaying τ leptons are reconstructed with the hadron-plus-strips algorithm [86, 87], which is seeded with anti- k_T jets with $p_T > 14$ GeV. This algorithm reconstructs τ_h candidates based on the number of tracks and the number of ECAL strips with energy deposits within the associated η - ϕ plane and reconstructs one-prong, one-prong+ π^0 (s), and three-prong decay modes (where a “prong” refers to a charged hadron constituent). For this analysis, a DNN discriminator is used to identify hadronic decays of τ leptons [88]. The input variables to the DNN include variables related to the τ_h isolation, τ_h lifetime, and other detector-related variables. These variables serve as input to a DNN, which provides an output discriminant. The threshold on the output discriminant depends on the τ_h p_T and provides a τ_h identification (ID) and reconstruction efficiency of about 60%. Two other DNNs are used to reject electrons and muons misidentified as τ_h candidates using dedicated criteria based on the consistency between the measurements in the tracker, the calorimeters, and the muon detectors.

The \vec{p}_T^{miss} is defined as the negative vector sum of the p_T of all PF candidates [89]. Its magnitude is referred to as p_T^{miss} .

The invariant mass of the $\tau\tau$ system $m_{\tau\tau}$ is a key variable for separating H candidate events from the background in this analysis. The $m_{\tau\tau}$ is reconstructed using the FASTMTT algorithm, which is similar to the SVFIT algorithm [90] used in previous CMS publications, except that it uses a simplified mass likelihood function to reduce the computation time. This algorithm makes use of the \vec{p}_T^{miss} and its uncertainty and the four-vectors of the reconstructed visible τ decay products to calculate an estimate of the mass of the parent boson and the full four-momenta of the H decay products needed to calculate MELA kinematic observables discussed in Section 3. Compared to the procedure described in Ref. [90], the FASTMTT algorithm removes the contributions of the leptonic and hadronic τ decay matrix elements to the likelihood function, and assumes that the neutrinos are collinear to the visible τ leptons. This gives a similar $m_{\tau\tau}$ resolution as the SVFIT algorithm, but the computation time is reduced by two orders of magnitude.

6.1 Event categorization

Selected events are classified according to four decay channels, $e\mu$, $e\tau_h$, $\mu\tau_h$, and $\tau_h\tau_h$, where e and μ indicate τ decays into electrons and muons, respectively. The resulting event samples are made mutually exclusive by discarding events that have additional loosely identified and

isolated electrons or muons. In cases where multiple pairs can be formed due to the presence of additional τ_h candidates, we select the pair that includes the τ_h candidate(s) with the largest value of the τ_h ID discriminant.

The largest irreducible source of background is Drell–Yan production of $Z/\gamma^* \rightarrow \tau\tau$, while the dominant background sources with jets misidentified as leptons are QCD multijet and W +jets. Other contributing background sources are $t\bar{t}$, single top quark, $Z/\gamma^* \rightarrow ee$, $Z/\gamma^* \rightarrow \mu\mu$, and diboson production.

The two τ lepton candidates assigned to the H decay are required to have opposite charges. Events are selected online using a combination of single-lepton, lepton+ τ_h , double- τ_h , and electron+muon triggers. The trigger requirements, geometrical acceptances, and p_T criteria are summarized in Table 3. The p_T thresholds in the selections are optimized to increase the sensitivity to the $H \rightarrow \tau\tau$ signal, while also satisfying the trigger requirements. The η selections are driven by reconstruction and trigger requirements.

Table 3: Kinematic selection requirements for the four di- τ decay channels. The trigger requirement is defined by a combination of trigger candidates with p_T over a given threshold, indicated inside parentheses in GeV. The pseudorapidity thresholds come from trigger and object reconstruction constraints. The p_T thresholds for the lepton selection are driven by the trigger requirements, except for the τ_h candidate in the $\mu\tau_h$ and $e\tau_h$ channels, and the sub-leading lepton in the $e\mu$ channel, where they have been optimized to increase the analysis sensitivity.

Channel	Trigger requirement	Year	Selection criteria		
			p_T (GeV)	η	Isolation
$\tau_h\tau_h$	$\tau_h(35) \& \tau_h(35)$	2016	$p_T^{\tau_h} > 40$	$ \eta^{\tau_h} < 2.1$	DNN τ_h ID
	$\tau_h(40) \& \tau_h(40)$	2017, 2018			
$\mu\tau_h$	$\mu(22)$	2016	$p_T^\mu > p_T^{\text{trigger}} + 1 \text{ GeV}$	$ \eta^\mu < 2.1$	$I^\mu < 0.15$
	$\mu(19) \& \tau_h(21)$	2016	$p_T^{\tau_h} > 30$	$ \eta^{\tau_h} < 2.3$	DNN τ_h ID
	$\mu(24)$	2017, 2018			
	$\mu(20) \& \tau_h(27)$	2017, 2018			
$e\tau_h$	$e(25)$	2016	$p_T^e > p_T^{\text{trigger}} + 1 \text{ GeV}$	$ \eta^e < 2.1$	$I^e < 0.15$
	$e(27)$	2017	$p_T^{\tau_h} > 30$	$ \eta^{\tau_h} < 2.3$	DNN τ_h ID
	$e(32)$	2018			
	$e(24) \& \tau_h(30)$	2017, 2018			
$e\mu$	$e(12) \& \mu(23)$	all years	$p_T^e > 15, p_T^\mu > 24$	$ \eta^e < 2.4$	$I^e < 0.15$
	$e(23) \& \mu(8)$	all years	$p_T^\mu > 15, p_T^e > 24$	$ \eta^\mu < 2.4$	$I^\mu < 0.15$

In the $\ell\tau_h$ channels, the large W +jets background is reduced by requiring the transverse mass, m_T , to be less than 50 GeV. The m_T is defined as follows,

$$m_T \equiv \sqrt{2p_T^\ell p_T^{\text{miss}}[1 - \cos(\Delta\phi)]}, \quad (14)$$

where p_T^ℓ is the transverse momentum of the electron or muon and $\Delta\phi$ is the azimuthal angle between the lepton momentum and \vec{p}_T^{miss} .

In the $e\mu$ and $\ell\tau_h$ channels, events with b jets are vetoed to reduce the background from $t\bar{t}$ production. In the $e\mu$ channel, this background is further mitigated by requiring $p_\zeta = p_\zeta^{\text{miss}} - 0.85 p_\zeta^{\text{vis}} > -35 \text{ GeV}$, where p_ζ^{miss} is the component of \vec{p}_T^{miss} along the bisector of the p_T of the two leptons and p_ζ^{vis} is the sum of the components of the lepton p_T along the same direction [91].

Event categories are designed to increase the sensitivity to the signal by isolating regions with

large signal-to-background ratios, and to provide sensitivity to the Hgg and HVV parameters. They follow closely the selection in Ref. [92]:

- 0-jet category: This category targets H events produced via ggH. Events containing no jets with $p_T > 30$ GeV are selected.
- VBF category: This category targets H events produced via the VBF process and ggH in association with two jets. Events are selected with at least two jets with $p_T > 30$ GeV. In the $e\mu$ and $\ell\tau_h$ channels the invariant mass of the two leading jets m_{jj} is required to be larger than 300 GeV. In the $\tau_h\tau_h$ channel we require the separation $|\Delta\eta_{jj}|$ between the two leading jets to be greater than 2.5, and the transverse component of the vector sum of the \vec{p}_T^{miss} and the \vec{p}_T of the visible decay products of the τ leptons, defined as $\vec{p}_T^{\tau\tau}$, to have a magnitude ($p_T^{\tau\tau}$) greater than 100 GeV.
- Boosted category: This category contains all the events that do not enter one of the previous categories, namely events with one jet and events with several jets that fail the requirements of the VBF category. It targets events with an H produced in ggH and recoiling against an initial-state radiation jet.

7 Background estimation

In this section we describe the background processes to the $H \rightarrow \tau\tau$ signal and methods to estimate their contributions. The major background is from Drell–Yan production, where the Z boson decays to a pair of τ leptons, followed by backgrounds from jets misidentified as τ lepton candidates. Whenever possible we rely on data to estimate background contributions. The data, signal, and background predictions in the VBF category are illustrated in Fig. 2.

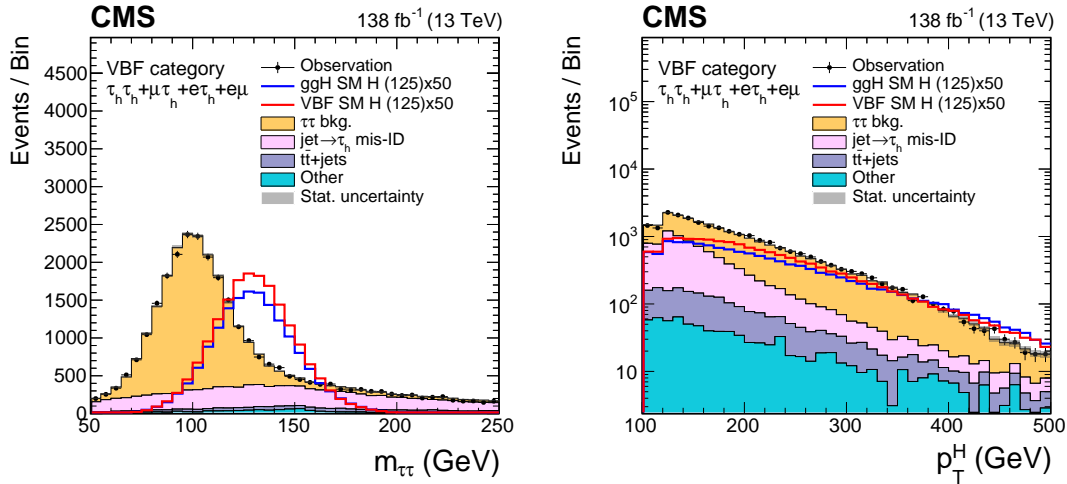


Figure 2: The $m_{\tau\tau}$ (left) and p_T (right) distributions for H candidate di- τ lepton pairs in the VBF category. All events selected in the $e\mu$, $e\tau_h$, $\mu\tau_h$, and $\tau_h\tau_h$ final states are included. The yields of the H processes are scaled to match 50 times the SM predictions. Only statistical uncertainties are shown.

7.1 Backgrounds due to $\tau\tau$ events

The Drell–Yan $Z/\gamma^* \rightarrow \tau\tau$ process is the dominant background to the $H \rightarrow \tau\tau$ signal as both processes share the same final state and have very similar kinematic properties. Additionally, several other process such as $t\bar{t}$ can produce a $\tau\tau$ final state. Given the dominance of these

backgrounds in data, we rely on an embedding method [93] to simulate them: in a dedicated control region, $Z/\gamma^* \rightarrow \mu\mu$ candidate events are selected from data; calorimeter deposits and tracks produced by the pair of muons in the event are removed; the muons in the event are replaced with simulated τ leptons with the same kinematic properties as the removed muons; and the PYTHIA generator is used to model the decay of the τ leptons in the same way as a typical $Z/\gamma^* \rightarrow \tau\tau$ decay.

The embedding process is performed separately for each decay channel and results in greatly improved statistical accuracy compared to that of a typical MC simulation. Using data to describe effects such as pileup and detector noise results in a much more reliable description of p_T^{miss} and jet related variables, which in turn reduces systematic uncertainties arising from, e.g., jet energy corrections.

7.2 Background due to jet misidentification

One of the major backgrounds to the $H \rightarrow \tau\tau$ signal in the $e\tau_h$, $\mu\tau_h$, and $\tau_h\tau_h$ channels originates from events where a jet is misidentified as a τ_h candidate. We refer to such backgrounds as $\text{jet} \rightarrow \tau_h$ processes. The background processes include QCD multijet production, W +jets, $t\bar{t}$, and diboson processes. As the $\text{jet} \rightarrow \tau_h$ misidentification rates are typically $\sim 0.1\text{--}1\%$, the use of MC simulation to model this background is undesirable due to the statistical limitation and systematic uncertainty associated with the correct modeling of the detector response to jets identified as τ leptons. Thus, we rely on data to model this background, using the “fake factors” (F_F) method [94].

To estimate the $\text{jet} \rightarrow \tau_h$ contamination in the signal region we select τ_h candidates that fulfill all event selection criteria with the exception of containing τ_h candidates that fail the nominal identification requirements but pass a looser requirement on the DNN. This selection is referred to in the following as “relaxed”. In the $\tau_h\tau_h$ channel, either one or both τ_h may originate from a $\text{jet} \rightarrow \tau_h$ but the dominant process is multijet QCD, which results in two $\text{jet} \rightarrow \tau_h$ candidates. In this case, we require only that the leading τ_h fail the nominal identification. These selected events are then scaled on an event-by-event basis by the F_F , which are ratios between the nominal and relaxed τ_h identification rates.

The F_F are determined separately for each channel, and for each of the dominant processes contributing to the $\text{jet} \rightarrow \tau_h$ background. For the $\tau_h\tau_h$ channel, the $\text{jet} \rightarrow \tau_h$ background originates almost entirely from QCD multijet events, and therefore F_F are derived only for this process. For the $e\tau_h$ and $\mu\tau_h$ channels, separate F_F are derived for QCD multijet, W +jets, and $t\bar{t}$ processes. The QCD and W +jets F_F are measured in dedicated control regions enriched with the events from the given process. The QCD control region is defined by inverting the opposite-sign charge requirement on the di- τ candidate pair. The W +jets control region is defined by selecting events with $m_T > 70$ GeV. Obtaining a $t\bar{t}$ control region with high purity is not possible, and the F_F are therefore measured in simulation for this subdominant process. For all control regions, we subtract the contributions of events with τ_h candidates arising from genuine hadronic τ decays or from misidentified electrons or muons using simulations. We parameterize the F_F as a function of the τ_h p_T . As events in this study are categorized primarily by the number of jets in the event, the F_F are measured in jet multiplicity bins: no jets, one jet, and two or more jets.

The F_F for each of the individual processes are then weighted into the overall F_F to account for their relative contributions to the events in the relaxed identification region. For this purpose, simulated events are used to determine the expected contributions of W +jets and $t\bar{t}$ events, and the QCD contribution is estimated by subtracting all simulated non-QCD processes from

the data. For the $e\tau_h$ and $\mu\tau_h$ channels, the F_F measured for the W +jets process are weighted to also account for all other subdominant $\text{jet} \rightarrow \tau_h$ processes (all processes except multijet QCD, W +jets, and $t\bar{t}$). For the $\tau_h\tau_h$ channel, the multijet QCD F_F account also for all other subdominant processes where the leading τ_h candidate is a misidentified jet. The events in which the subleading τ_h candidate is a misidentified jet and the leading τ_h candidate is a genuine τ lepton are modeled via simulation; these events constitute only a small fraction ($\mathcal{O}(2\%)$) of the total misidentified jet background in this channel.

Finally, the F_F are further corrected to accommodate residual differences observed when applying the measured F_F to events in control regions. Such corrections are needed to account for: differences in the $\text{jet} \rightarrow \tau_h$ misidentification rates in control and signal regions arising from, for example, slight differences in the jet flavor compositions, the choices of functional forms for parameterizing the p_T dependence, the finite binning of the parameterizing variables, and the omission of dependencies on kinematic or topological variables, such as η for which F_F values are averaged out. Sub-leading dependencies of the F_F on p_T^ℓ and m_T for the $\ell\tau_h$ channels, or the p_T of the subleading τ_h candidate and the mass of the visible $\tau\tau$ decay products for the $\tau_h\tau_h$ channel, enter via these corrections.

In the $e\mu$ channel, one of the minor backgrounds stems from the multijet QCD process, where at least one jet is misidentified as an electron or a muon candidate. The majority of these events involve $b\bar{b}$ production, with electron and muon candidates produced in semileptonic decays of heavy-flavor quarks. This background is estimated from a sideband region using events with an electron and a muon with same-sign (SS) electric charges. Scale factors are then applied to extrapolate from this sideband region to the signal region, where the electron and the muon have opposite-sign (OS) electric charges. These so-called OS/SS scale factors are derived from a control region where the muons pass a relaxed isolation requirement but fail the signal region isolation criteria. The dependence of the OS/SS factors on the ΔR between the two leptons and jet multiplicity in the event is taken into account. A correction is also applied to account for any bias introduced by the inversion of the isolation requirement on the muon candidate. Finally, we subtract contributions from known SM processes using embedded and MC simulation samples.

7.3 Other background processes

The remaining backgrounds include Drell–Yan processes, where the Z boson decays to a pair of electrons or muons and one or more of the final state leptons is misidentified as the τ lepton, as well as $t\bar{t}$, single top quark and multiboson production with fewer than two genuine τ leptons and additional electrons or muons that are misidentified as leptonically or hadronically decaying τ leptons. These backgrounds are small and we rely on MC simulation to estimate their contribution to the signal region. To avoid double-counting of backgrounds arising from jet misidentification, we remove the events with the generator-level quark or gluon matched to the reconstructed τ lepton candidate in the final state. Similarly, Drell–Yan MC events as well as any other MC simulation events with two genuine τ leptons are discarded to avoid overlap with the embedded samples.

7.4 Corrections to simulated data

To improve the agreement between the signal and background processes modeled with simulations and the data, the following corrections are applied to the simulated events (including $\tau\tau$ -embedded events for corrections pertaining to the simulated τ leptons):

- The pileup distribution in simulation is reweighted in order to match the pileup in

data.

- The electrons and muons channels are corrected to account for their trigger efficiencies, reconstruction, identification, and isolation requirements. The channels containing τ_h candidates are corrected for their trigger efficiencies, reconstruction, and identification requirements. Corrections are also applied to events including $e \rightarrow \tau_h$ and $\mu \rightarrow \tau_h$ candidates to account for differences in the misidentification probabilities.
- For the $e\mu$ and $\ell\tau_h$ channels, corrections are applied to account for differences in the number of events passing the b jet veto, as a result of variations in the probabilities for jets to be tagged as b jets.
- The τ_h energy scales are corrected per decay mode to match the energy scale in data using the $Z/\gamma^* \rightarrow \tau\tau$ visible mass peak. Separate corrections are derived for τ_h candidates that originate from genuine hadronically decaying τ leptons and those that originate from electron and muon misidentifications. The electron energy scale is adjusted in data and simulation using the Z boson mass peak, and the resolution of the simulated electrons is also adjusted to match the data.
- Jet energy scale corrections are applied to both data and simulated events, and the energy resolution of simulated jets is adjusted to match the resolution in data. For the Drell-Yan, W+jets, and H events estimated from simulation, corrections are applied to the p_T^{miss} based on the vector difference of the measured p_T^{miss} and the total p_T of the neutrinos from the Z, W, or H decay products ("recoil corrections").
- The Z boson mass and p_T spectra in simulation are corrected to better match the data. To this purpose the Z mass and p_T are measured in data and simulation in di-muon events. The observed differences between the data and simulations are taken as event weights that are subsequently applied to the simulated $Z/\gamma^* \rightarrow \ell\ell$ events. The size of the corrections are typically less than 20%. For $t\bar{t}$ events, the top quark p_T spectra are also reweighted to match the p_T spectra in data. The procedure used to derive these corrections is described in Ref. [95]. The sizes of the corrections are less than 20%.
- During the 2016–2017 data-taking, a gradual shift in the timing of the inputs of the ECAL L1 trigger in the region at $|\eta| > 2.0$ caused a specific trigger inefficiency [96]. For events containing an electron (a jet) with p_T larger than ≈ 50 GeV (≈ 100 GeV), in the region $2.5 < |\eta| < 3.0$ the efficiency loss is ≈ 10 –20%, depending on p_T , η , and time. Correction factors were computed from data and applied to the acceptance evaluated by simulation to account for this inefficiency. This results in a small decrease in the estimated signal and background yields, e.g., the inclusive SM VBF yields are reduced by about 2–3%.

8 Systematic uncertainties

A variety of systematic uncertainties are taken into account in the analysis. The uncertainty model consists of normalization uncertainties that only scale the yield of a distribution while leaving its shape unchanged, and shape uncertainties that also alter the shapes of the distributions. The leading systematic uncertainty sources result from the jet energy scales and resolutions, and the statistical uncertainties in the background predictions. All systematic uncertainties are implemented in the form of nuisance parameters in the likelihood, which can be further constrained by the fit to the data. The uncertainties considered in this analysis are summarized in Table 4 and detailed below.

Table 4: Sources of systematic uncertainties.

Source	Uncertainty
τ_h ID	p_T /decay-mode dependent (3–10%)
τ_h separation from e/μ	3%
$e \rightarrow \tau_h$ ID	η dependent (9–40%)
$\mu \rightarrow \tau_h$ ID	η dependent (10–70)%
e ID	2%
μ ID	1%
b jet veto	0–10%
Integrated luminosity	1.6%
Trigger	2% for e/μ , p_T /decay-mode dep. for τ_h ($\mathcal{O}(10\%)$)
$t\bar{t}$ cross section	4.2%
Diboson cross section	5%
Single top quark cross section	5%
Drell–Yan cross section	2%
L1 trigger timing (2016 and 2017)	Event-dependent (0.2–15%)
$\mathcal{B}(H \rightarrow \tau\tau)$	2.1%
τ_h energy scale	Decay-mode dependent (0.2–1.2%)
$e \rightarrow \tau_h$ energy scale	Decay-mode dependent (1–7%)
$\mu \rightarrow \tau_h$ energy scale	1%
Electron energy scale	p_T/η dependent ($< 1.25\%$)
Muon energy scale	η dependent 0.4–2.7%
Jet energy scale	p_T/η dependent (0.5–14%)
Jet energy resolution	η dependent (2–95%)
p_T^{miss} unclustered energy scale	Event-dependent (0–20%)
p_T^{miss} recoil corrections	0.3–5.8%
Jet $\rightarrow \tau_h$ misidentification	Event-dependent ($\mathcal{O}(10\%)$)
QCD multijet in the $e\mu$ channel	Event-dependent ($\mathcal{O}(20\%)$)
Embedded yield	4%
$t\bar{t}$ in embedded	10%
Signal theoretical uncertainty	Event-dependent (up to 25%)
Top quark p_T reweighting	p_T dependent (0–21%)
Drell–Yan p_T and mass reweighting	p_T /mass dependent (0–11%)

The integrated luminosities of the 2016, 2017, and 2018 data-taking periods are individually known with uncertainties in the 1.2–2.5% range [54–56], while the total Run 2 (2016–2018) integrated luminosity has an uncertainty of 1.6%, the improvement in precision reflecting the (uncorrelated) time evolution of some systematic effects. The uncertainty in the L1 ECAL trigger timing correction factors described in Section 7 ranges 0.2–15%.

The uncertainties in the (electron) muon reconstruction, identification, and isolation efficiencies amount to (2) 1%. The electron and muon triggers contribute an additional 2% uncertainty in the yield of simulated processes. The uncertainty in the electron energy scale depends on p_T and η and is typically less than 1%. The muon energy scale uncertainty varies between 0.4 and 2.7% depending on η .

The τ_h reconstruction and identification efficiency is measured in three p_T bins (30–35, 35–40, > 40 GeV) or four τ_h decay mode bins and its uncertainty is dominated by the statistical component. The uncertainty is taken to be uncorrelated for the individual measurements and is within the 3–10% range. In addition, a yield uncertainty of 3% is taken into account for

genuine τ_h candidates due to the discrimination against electrons and muons. An additional uncertainty is applied for the τ_h reconstruction in the embedded samples to account for differences in the charged hadrons and π^0 reconstruction efficiencies, which ranges from 0.8 to 3%. The uncertainty in the τ_h trigger efficiencies depends on the p_T and decay mode of the τ_h candidates, and is therefore treated as a shape uncertainty. The magnitude of this uncertainty is typically $\mathcal{O}(10\%)$. For electrons and muons misidentified as τ_h candidates, an uncertainty derived in bins of p_T , η , and decay mode of the misidentified τ_h candidate is applied and amounts to between 9–40% and 10–70%, respectively. The uncertainty in the τ_h energy scale ranges from 0.2 to 1.1% depending on the decay mode. For electrons and muons misidentified as τ_h candidates, the uncertainty in the energy scale amounts to 1–6.5% for electrons and 1% for muons.

Uncertainties in the jet energy scale come from different sources and with partial correlations. These sources typically affect different regions of the detector and their magnitude depends on the jet p_T and η . The collective magnitude of these uncertainties per jet typically ranges 0.5–14%. Uncertainties in the jet energy resolution are also taken into account and range from 2 to 95% per jet depending on η . The jet energy scale and resolution uncertainties create migrations between categories defined on the basis of the jet multiplicity or m_{jj} , and affect the shapes of the $\Delta\phi_{jj}$ and MELA discriminants. For all MC samples without recoil corrections applied, the uncertainties in the jet energy scale and resolution are also propagated to the \vec{p}_T^{miss} .

For simulated events that have recoil corrections, the uncertainties in the resolution and response of the \vec{p}_T^{miss} are derived as part of the estimate of the recoil corrections and range from 0.3 to 5.8%. Other processes suffer from uncertainties in the energy measurement for the energy depositions in the calorimeter, not associated with jets and photon candidates, so-called unclustered energy scale uncertainties. The magnitudes of these uncertainties depend on the p_T , η , and types of the unclustered PF candidates. The overall sizes of these uncertainties are typically less than 20%.

The yield uncertainty related to discarding events with a b-tagged jet varies up to 10% for backgrounds with heavy-flavor jets, whereas for backgrounds with mostly gluon and light-flavor jets it is less than 1%.

For background with jet $\rightarrow \tau_h$ misidentifications, the uncertainties in the measured F_F are propagated to the background predictions as shape uncertainties. This includes statistical uncertainties in the fitted functions as well as systematic uncertainties coming from residual differences observed in control regions. Altogether the uncertainties on the F_F are $\mathcal{O}(10\%)$. Similarly, for the multijet QCD estimation in the $e\mu$ channel uncertainties in the OS/SS extrapolation factors are taken into account. Altogether the uncertainties amount to $\mathcal{O}(20\%)$.

Uncertainties related to the embedding method are taken into account in addition to those pertaining to the simulated τ lepton decay products described previously. Embedded samples include all events with two τ lepton candidates, essentially Drell–Yan events, but also contain small fractions of diboson and $t\bar{t}$ events. A shape uncertainty is applied to take into account the contamination from these non Drell–Yan events, which amounts to 10% of the $t\bar{t}$ and diboson contribution to embedded samples, as estimated from simulation. Data events with muons are selected with a muon trigger before embedding the simulated τ leptons. The uncertainty in this trigger requirement amounts to 4%.

Uncertainties in the $t\bar{t}$, Drell–Yan, diboson, and single top quark production cross sections amount to 4.2, 2.0, 5.0, and 5.0%, respectively. This includes uncertainties due to missing higher-order corrections, the PDFs, and α_s . For the $t\bar{t}$ cross section the uncertainty in the top

quark mass is also included. Uncertainties due to the reweighting of the top p_T and Drell–Yan p_T and mass spectra are also included. For the $t\bar{t}$ samples, the size of the correction is taken as the uncertainty, while for the Drell–Yan samples, the correction is varied by 10%.

The theoretical uncertainties in the H production cross sections and $H \rightarrow \tau\tau$ branching fraction follow the recommendations in Ref. [48]. The uncertainty in the branching fraction of the H to τ leptons includes a 1.7% uncertainty due to missing higher-order corrections, a 1% parametric uncertainty in the quark masses, and a 0.62% parametric uncertainty in α_s . The inclusive uncertainty related to the PDFs amounts to 3.2, 2.1, 1.8, and 1.3%, respectively, for the ggH, VBF, WH, and ZH production modes. Acceptance uncertainties for the ggH signal due to renormalization and factorization scale variations are applied following the uncertainty schemes proposed in Ref. [48]. The sizes of these uncertainties are typically smaller than 25%. Acceptance uncertainties for the VBF signal due to renormalization and factorization scale variations are applied as yield uncertainties. The sizes of the uncertainties are typically smaller than 5%.

Uncertainties arising from the limited sample size of the simulated events, or data control regions, are taken into account using the “Barlow–Beeston” method [97, 98]. They are considered for all bins of the distributions used to extract the results.

9 Analysis of ggH production

In this section we first review the analysis methods employed to extract the Hgg anomalous coupling parameters. In Section 9.1 we describe the MELA method from which we obtain our most stringent expected limits on the anomalous coupling parameters. The $\Delta\phi_{jj}$ method, which is used to cross check the results obtained by the MELA method, is briefly described in Section 9.2. The results obtained are then presented in Section 9.3.

9.1 The MELA method

For events entering the VBF category, a combination of simple neural networks and MELA discriminants is used. The former provide optimal separation of the dominant backgrounds for a given channel from the H production, while the latter offer powerful handles to distinguish different signal hypotheses.

A feed-forward network containing two hidden layers is used in each channel. As dominant backgrounds vary by channel, the observables used in the neural network training change and therefore the architecture of the network is modified for each channel. The number of nodes per layer is kept to a minimum to reduce the complexity of the neural network without compromising its performance. As sensitivity to the Hgg anomalous coupling is maximal for events with kinematics similar to those of VBF production, we use VBF signal events as the signal process for all neural networks. This provides the added benefit that the same network can be used in the analysis of both ggH and VBF production processes.

The simplest neural network is employed in the $e\tau_h$ and $\mu\tau_h$ channels where the background is dominated by the $Z/\gamma^* \rightarrow \tau\tau$ production. Thus, a simple binary classifier is trained to distinguish VBF production from the $Z/\gamma^* \rightarrow \tau\tau$ process. We use all seven MELA input variables (Ω^{assoc}) defined for the VBF process in Section 3, $m_{\tau\tau}$, m_{jj} , and $p_T^{\tau\tau}$ as input features for the network.

Multiclass neural networks are utilized in the $\tau_h\tau_h$ and $e\mu$ channels because of the presence of two dominant backgrounds in each channel. In the $\tau_h\tau_h$ channel, a network is trained to distinguish events in three classes: events that are likely to be from the $Z/\gamma^* \rightarrow \tau\tau$ produc-

tion, VBF H production, and background events from processes with jets misidentified as τ_h candidates, using the same features as the $\ell\tau_h$ network. For the $e\mu$ channel, the network is trained to classify events into three classes: $Z/\gamma^* \rightarrow \tau\tau$, VBF, and $t\bar{t}$. The $e\mu$ channel utilizes the same features as the $\ell\tau_h$ network, but also includes the jet multiplicity and p_ζ .

For the binary classifiers we use the neural network output scores as discriminating variables, whereas for the multiclass networks we use the output scores for the VBF signal classes. We will refer to these discriminants collectively as \mathcal{D}_{NN} .

Three MELA discriminants are used in the Hgg analysis. In order to separate ggH production from VBF production, $\mathcal{D}_{2\text{jet}}^{\text{VBF}}$ as defined in Eq. (15) is used. The discriminant $\mathcal{D}_{0-}^{\text{ggH}}$, defined in Eq. (16), is used to separate ggH produced with the SM couplings from ggH produced with a pure pseudoscalar coupling. Lastly, $\mathcal{D}_{CP}^{\text{ggH}}$, defined in Eq. (17), provides sensitivity to the interference between the CP -odd and CP -even contributions:

$$\mathcal{D}_{2\text{jet}}^{\text{VBF}} = \frac{\mathcal{P}_{\text{SM}}^{\text{ggH}} + \mathcal{P}_{0-}^{\text{ggH}}}{\mathcal{P}_{\text{SM}}^{\text{ggH}} + \mathcal{P}_{0-}^{\text{ggH}} + \mathcal{P}_{\text{SM}}^{\text{VBF}}}, \quad (15)$$

$$\mathcal{D}_{0-}^{\text{ggH}} = \frac{\mathcal{P}_{\text{SM}}^{\text{ggH}}}{\mathcal{P}_{\text{SM}}^{\text{ggH}} + \mathcal{P}_{0-}^{\text{ggH}}}, \quad (16)$$

$$\mathcal{D}_{CP}^{\text{ggH}} = \frac{\mathcal{P}_{\text{SM}-0-}^{\text{ggH}}}{\mathcal{P}_{\text{SM}}^{\text{ggH}} + \mathcal{P}_{0-}^{\text{ggH}}}. \quad (17)$$

The results of the analysis are extracted with a global maximum likelihood fit based on signal-sensitive observables. We summarize the observables utilized in the analysis of the ggH production in Table 5. As the same set of observables is used in the HVV study, except for the superscripts of anomalous coupling specific MELA discriminators, we define them in Table 5 as well.

Table 5: List of observables used in the MELA method.

Category	Observable	Goal
0-jet	$m_{\tau\tau}$	Separate H signal from backgrounds
Boosted	$p_T^{\tau\tau}, m_{\tau\tau}$	Separate H signal from backgrounds and BSM from SM HVV
VBF	\mathcal{D}_{NN}	Separate VBF-like H signal from backgrounds
VBF	$\mathcal{D}_{2\text{jet}}^{\text{VBF}}$	Separate ggH from VBF H production
VBF	$\mathcal{D}_{0-}^{\text{ggH}} (\mathcal{D}_{0-})$	Separate BSM from SM Hgg (HVV)
VBF	$\mathcal{D}_{CP}^{\text{ggH}} (\mathcal{D}_{CP}^{\text{VBF}})$	Sensitive to the interference between the CP -even and CP -odd contributions to the Hgg (HVV) coupling

We use four observables in total to construct fitted distributions in the VBF category: $\mathcal{D}_{0-}^{\text{ggH}}$, $\mathcal{D}_{CP}^{\text{ggH}}$, \mathcal{D}_{NN} , and $\mathcal{D}_{2\text{jet}}^{\text{VBF}}$. The selected events are binned in multidimensional histograms (templates) of these observables. The binning of these templates has been optimized to ensure sufficient statistical populations of all bins, to retain kinematic information, and for memory usage and speed of computer calculations.

The inclusion of the $\mathcal{D}_{CP}^{\text{ggH}}$ observable is intended to bring sensitivity to the sign of the interference between the CP -even and CP -odd contributions, which would manifest as an asymmetry between the number of events detected with positive and negative values of $\mathcal{D}_{CP}^{\text{ggH}}$. We

therefore include two bins in this discriminant, $\mathcal{D}_{CP}^{\text{ggH}} < 0$ and $\mathcal{D}_{CP}^{\text{ggH}} \geq 0$. It should be noted that $\mathcal{D}_{CP}^{\text{ggH}}$ is symmetric about $\mathcal{D}_{CP}^{\text{ggH}} = 0$ in the absence of CP -violation, and this symmetry is enforced for the background and CP -conserving signal templates to reduce the influence of statistical fluctuations. For the remaining three observables we allocate more bins to those that have a stronger influence on the expected sensitivity. For the $\ell\tau_h$ channels, we use 10, 8, and 4 equally sized bins for $\mathcal{D}_{0-}^{\text{ggH}}$, \mathcal{D}_{NN} , and $\mathcal{D}_{2\text{jet}}^{\text{VBF}}$, respectively. For the $e\mu$ channel, which is the least sensitive channel in this analysis, we respectively use 3, 2, and 4 bins for these observables. In all cases, neighboring bins are merged such that the background prediction has no bins with statistical uncertainty larger than 50% to prevent cases where bins have very low statistical populations. For the $\tau_h\tau_h$ channel, it was not possible to define a suitable set of equally spaced bins that fulfilled the optimization criteria. Therefore, we employ variable bin widths for the $\mathcal{D}_{0-}^{\text{ggH}}$, \mathcal{D}_{NN} , and $\mathcal{D}_{2\text{jet}}^{\text{VBF}}$ observables, and select bin boundaries that optimize the expected sensitivity, while minimizing the total number of bins in the templates.

We use two observables to construct our templates in the boosted category, $m_{\tau\tau}$ and $p_T^{\tau\tau}$, and one observable in the 0-jet category, $m_{\tau\tau}$. There are no dedicated MELA observables sensitive to anomalous couplings in these channels, as the events either have fewer than the two jets needed to construct the observables, or do not display significant separation between different signal scenarios to justify their inclusion. However, the $p_T^{\tau\tau}$ observable used in the boosted category has some sensitivity to anomalous HVV couplings, as the BSM VBF events generally have larger $p_T^{\tau\tau}$. Similarly, the relative yields of the signal events across categories also has some sensitivity to anomalous HVV couplings, as the signal acceptance in each category will vary depending on the p_T of the H. Despite not bringing any sensitivity to anomalous Hgg couplings, the 0-jet and boosted categories are included in the fit nonetheless to constrain backgrounds and to provide sensitivity to the inclusive ggH cross section. The chosen binning in these categories is thus similar to what was employed in previous CMS measurements [92].

Example distributions of the observables in the most sensitive $\tau_h\tau_h$ and $\mu\tau_h$ channels are given in Fig. 3.

9.2 The $\Delta\phi_{jj}$ method

This cross check method is based on the strategy proposed in Ref. [50]. The $\Delta\phi_{jj}$ variable, defined in Section 3.2, provides sensitivity to the CP properties of the Hgg vertex. The VBF-like ggH events are targeted as they have been shown to be most sensitive to the Hgg anomalous couplings [50].

The event selection and categorization follows closely those described in Section 6.1. The only notable differences are in the definitions of the VBF signal categories, which are therefore described below.

The VBF category definition described in Section 6.1 is adopted for the $e\mu$ and $\ell\tau_h$ channels. For the $\tau_h\tau_h$ channel, the VBF category selections defined previously for the $\ell\tau_h$ channels are utilized. The selected VBF-like events are then further subdivided into four categories based on m_{jj} and $p_T^{\tau\tau}$ to enhance the separation between different CP scenarios and to provide additional differentiation between the signal and backgrounds. The four categories are defined as follows: events with $m_{jj} < 500$ GeV and $p_T^{\tau\tau} < 150$ GeV (low- m_{jj} category); events with $m_{jj} < 500$ GeV and $p_T^{\tau\tau} \geq 150$ GeV (low- m_{jj} boosted category); events with $m_{jj} \geq 500$ GeV and $p_T^{\tau\tau} < 150$ GeV (high- m_{jj} category); and events with $m_{jj} \geq 500$ GeV and $p_T^{\tau\tau} \geq 150$ GeV (high- m_{jj} boosted category).

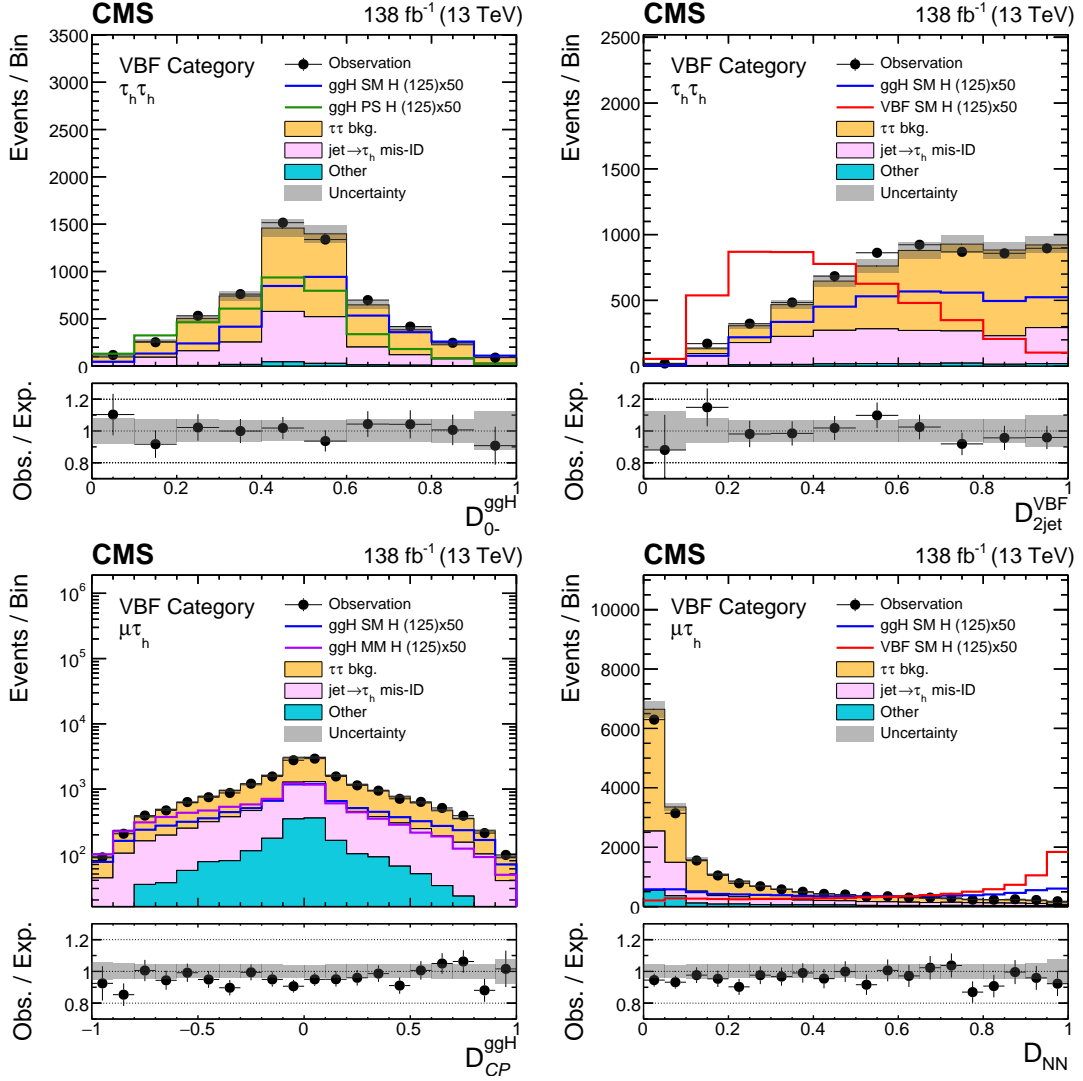


Figure 3: Examples of data and signal and background predictions for MELA and neural network discriminants in the $\tau_h \tau_h$ and $\mu \tau_h$ channels. Events passing the selections outlined in Section 6 and allocated to the VBF category are included. The yields of the H processes are scaled to match 50 times the SM predictions. The uncertainty band includes statistical uncertainties and systematic uncertainties that affect the normalization of the background distribution. The expectation in the ratio panel is the sum of the estimated backgrounds and the SM H signal. For the D_{0-}^{ggH} discriminant the distribution expected for a pseudoscalar H hypothesis (labeled "PS" in the legend) is overlaid to be compared to the SM signal. Similarly, for the D_{CP}^{ggH} discriminant the distribution for a CP -violating scenario with the maximum-mixing between CP -even and CP -odd couplings (labeled "MM" in the legend) is shown.

Table 6: List of observables used in the $\Delta\phi_{jj}$ method.

Category	Observable	Goal
0-jet	$m_{\tau\tau}$	Separate H signal from backgrounds
Boosted	$p_T^{\tau\tau}, m_{\tau\tau}$	Separate H signal from backgrounds
VBF	$m_{\tau\tau}$	Separate H signal from backgrounds
VBF	$\Delta\phi_{jj}$	Differentiate between CP -even, CP -odd, and mixed CP scenarios

We summarize the observables utilized in Table 6. In this case we use two-dimensional (2D) templates in the VBF categories to extract the results. These templates are constructed using the $\Delta\phi_{jj}$ and $m_{\tau\tau}$ observables. We use 12 equally-spaced bins for $\Delta\phi_{jj}$. Variable bin widths are used for the $m_{\tau\tau}$ observable, where the bin boundaries are selected to capture the peaking structures of the signal distributions close to $m_{\tau\tau} \sim 125$ GeV. The initial choice of the $m_{\tau\tau}$ bin boundaries is the same for all channels and categories but we apply an additional merging of neighboring bins in cases where the statistical fluctuations in the signal or background templates are excessive.

9.3 Results of the ggH analysis

The results are extracted by performing a binned maximum likelihood fit to the data combining all categories for the different channels and data-taking years. The likelihood function is defined as a product of conditional probabilities over all bins i :

$$\mathcal{L}(\text{data}|\mu_{\text{ggH}}, \mu_{\text{qqH}}, \vec{f}, \theta) = \prod_i \text{Poisson}(n_i | s_i(\mu_{\text{ggH}}, \mu_{\text{qqH}}, \vec{f}, \theta) + b_i(\theta)) \cdot p(\tilde{\theta}|\theta), \quad (18)$$

where n_i is the observed number of data events in each bin. The signal and background expectations are given by s_i and b_i respectively, which are functions of θ , that represents the full set of nuisance parameters corresponding to the systematic uncertainties, and the parameters that modify the H signal processes: μ_{ggH} , μ_{qqH} , and \vec{f} . The parameters μ_{ggH} and μ_{qqH} are the H signal strength modifiers that respectively modify the ggH and VBF+VH cross sections with respect to the SM values. The \vec{f} term represents the set of anomalous coupling parameters that modify the distributions of the ggH and/or VBF+VH signals. In the case of Hgg anomalous coupling measurements, $\vec{f} = (f_{a3}^{\text{ggH}}, f_{a3})$. Finally, the $p(\tilde{\theta}|\theta)$ term represents the full set of probability density functions of the uncertainties in the nominal values of the nuisance parameters $\tilde{\theta}$. The systematic uncertainties that affect only the normalizations of the signal and background processes are assigned log-normal external constraints, whereas the shape altering systematic uncertainties are assigned Gaussian external constraints. The negative log-likelihood is defined as

$$-2\Delta \ln \mathcal{L} = -2\Delta \ln \frac{\mathcal{L}(\text{data}|\mu_{\text{ggH}}, \mu_{\text{qqH}}, \vec{f}, \theta)}{\mathcal{L}(\text{data}|\hat{\mu}_{\text{ggH}}, \hat{\mu}_{\text{qqH}}, \vec{\hat{f}}, \hat{\theta})}, \quad (19)$$

with $\hat{\mu}_{\text{ggH}}$, $\hat{\mu}_{\text{qqH}}$, $\vec{\hat{f}}$, and $\hat{\theta}$ as the best fit values of the signal modifiers and nuisance parameters. The 68 and 95% confidence level (CL) intervals are identified when $-2\Delta \ln \mathcal{L} = 1.00$ and 3.84, respectively, for which exact coverage is derived using the asymptotic approximation [99].

The measurements of f_{a3}^{ggH} , or equivalently f_{CP}^{Htt} or α^{Hff} according to Eq. (10), is performed using the two methods based on MELA and $\Delta\phi_{jj}$. An example of a pre-fit distribution for the MELA method is given in Fig. 4 for one of the most sensitive signal categories. Fig. 5 shows the post-fit distribution in the VBF high- m_{jj} boosted category in the $\tau_h \tau_h$ channel, which is the

most sensitive category used to extract the results using the $\Delta\phi_{jj}$ method. The results of the likelihood scans are shown in Fig. 6–7 and listed in Table 7.

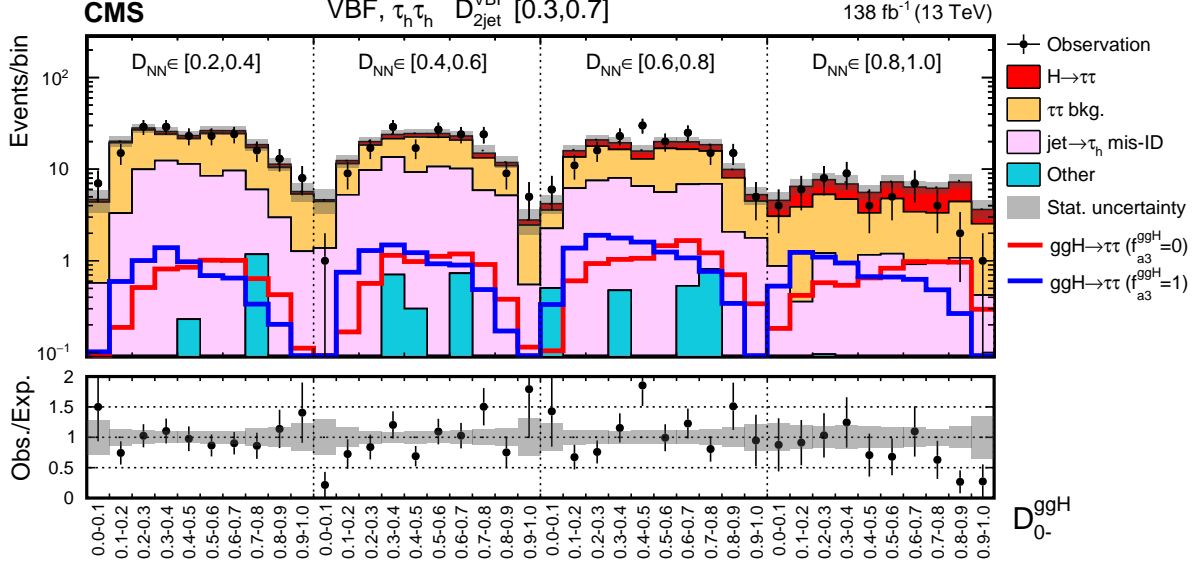


Figure 4: The observed and predicted 2D distribution of (D_0^{ggH}, D_{NN}) before the fit to data in the most sensitive VBF category region with $0.3 < D_{2jet}^{VBF} < 0.7$ in the $\tau_h \tau_h$ channel. The total H signal, including VBF, ggH, and VH processes, is shown stacked on top of the background in the solid red histogram. The ggH signal for the CP -even (CP -odd) scenario is also shown overlaid by the red (blue) line. Only the statistical uncertainties are included in the uncertainty band.

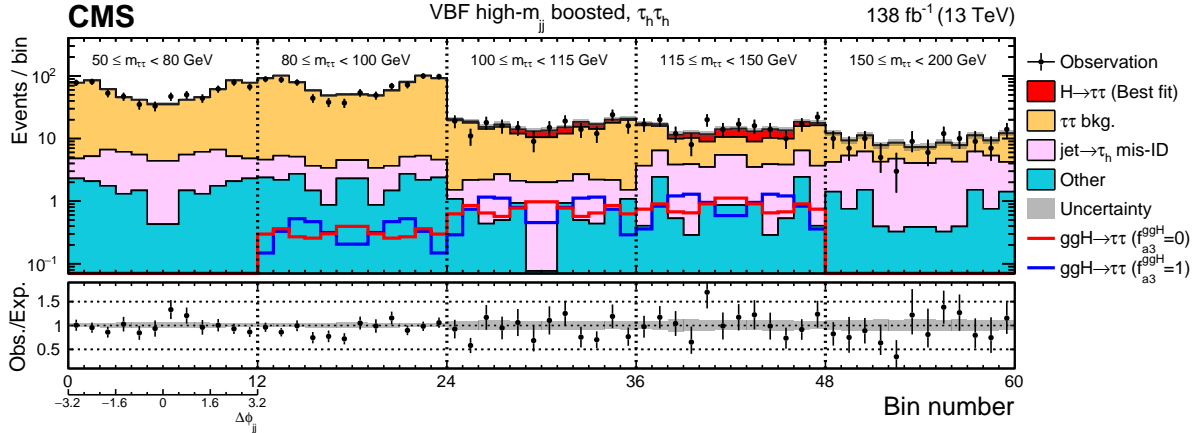


Figure 5: Observed and predicted 2D distributions after the fit to data in the VBF high- m_{jj} boosted category in the $\tau_h \tau_h$ channel. The total H signal, including VBF, ggH, and VH processes, is shown stacked on top of the background in the solid red histogram. The ggH signal for the CP -even (CP -odd) scenario is also shown overlaid by the red (blue) line. The uncertainty band accounts for all sources of systematic uncertainty in the signal and background predictions. The expectation in the ratio panel is the sum of the estimated backgrounds and the best fit signal.

For the MELA method, the maximum value of the $-2\Delta \ln \mathcal{L}$ is noticeably larger for the observed scan (occurring at $f_{a3}^{ggH} \approx -0.8$) compared to the expected. We checked and excluded a possibility that the discrepancy originated from artificial effects of our analysis procedure. We used

Table 7: Allowed 68% (central values with uncertainties) and 95% CL (in square brackets) intervals on anomalous Hgg coupling parameters using the $H \rightarrow \tau\tau$ decay. The use of “—” indicates cases where no exclusion at the 95% CL was found. As indicated in the Table, the results are presented for the MELA method, as well as the $\Delta\phi_{jj}$ method for comparison. The final results of this study are from the MELA method. The α^{Hff} results are derived from f_{a3}^{ggH} following Eqs. (5), (6), and (10).

Parameter	Method	Observed		Expected	
		68% CL	95% CL	68% CL	95% CL
f_{a3}^{ggH}	MELA	$0.08^{+0.35}_{-0.08}$	$[-0.09, 0.90]$	0.00 ± 0.36	—
f_{a3}^{ggH}	$\Delta\phi_{jj}$	$0.07^{+0.59}_{-0.19}$	—	0.00 ± 0.39	—
α^{Hff}	MELA	$(11^{+18}_{-10})^\circ$	$[-11, 63]$	$(0 \pm 26)^\circ$	—
α^{Hff}	$\Delta\phi_{jj}$	$(10^{+32}_{-24})^\circ$	—	$(0 \pm 27)^\circ$	—

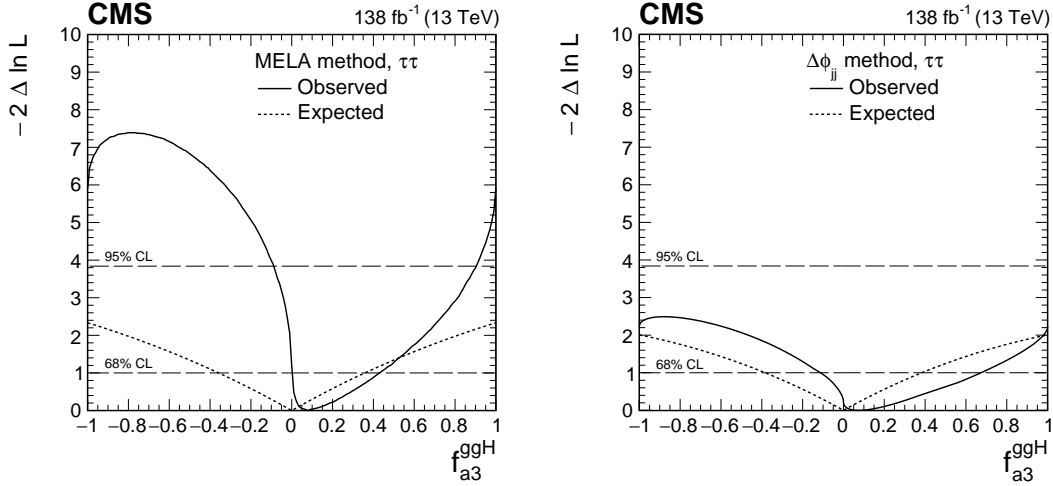


Figure 6: Observed (solid) and expected (dashed) likelihood scans of f_{a3}^{ggH} obtained with the MELA method (left) and the $\Delta\phi_{jj}$ method used as a cross check (right).

pseudo-experiments to estimate the probability of obtaining a maximum value of the $-2\Delta \ln \mathcal{L}$ greater than or equal to the maximum $-2\Delta \ln \mathcal{L}$ of the observed scan. This probability was determined to be 33%. We thus conclude that the observed results are affected by statistical fluctuations but compatible with the signal plus background model.

The use of the MELA method is shown to improve the expected uncertainty in f_{a3}^{ggH} (α^{Hff}) by 8 (4)%. This improvement owes partly to the use of neural networks that differentiate the H signal from the backgrounds more effectively, and partly to the inclusion of matrix-element discriminants that improve the separation between CP -even, CP -odd, and mixed CP scenarios. In the case of the ggH production, the SM process is generated by the quark loop represented by the a_2^{gg} term in Eq. (1). This makes it harder to distinguish the anomalous a_3^{gg} contribution from the SM, as both are generated by dimension-six operators and many of their kinematic features are similar. Most of the sensitivity to CP -odd couplings is primarily in the azimuthal correlation of two jets, which explains why the full multivariate MELA treatment of kinematic information does not bring as much additional information as in the case of the VBF production, described in the following section, where the SM process is generated by the tree-level coupling g_1^{VV} in Eq. (1), which is a dimension-four operator. This leads to kinematic differ-

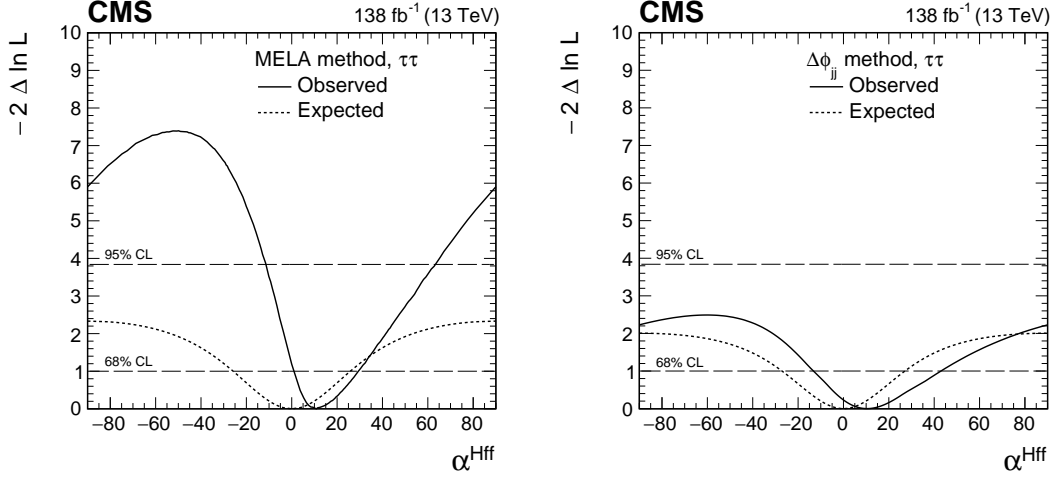


Figure 7: Observed (solid) and expected (dashed) likelihood scans of α^{Hff} (in degrees) obtained with the MELA method (left) and the $\Delta\phi_{jj}$ method used as a cross check (right).

ences between the anomalous contributions and the SM in multiple observables and a much larger gain from the full multivariate MELA treatment.

We also cross-checked the results neglecting CP -odd contributions to the VBF and VH processes (f_{a3} fixed to zero). This was found to have only a minor effect on the best fit value and uncertainty of $f_{a3}^{\text{ggH}}(\alpha^{\text{Hff}})$. Therefore, we present results only for the more general case where f_{a3} is unconstrained.

10 Analysis of VBF production

As MELA-based observables offer superior sensitivity and discrimination among different possible anomalous HVV couplings in the VBF and VH productions compared to single kinematic observables, such as $\Delta\phi_{jj}$, the VBF study is conducted with MELA-based observables only. As the sensitivity to VH anomalous effects is small with the present data set, the analysis is optimized for the VBF process. However, we allow the anomalous couplings to modify the VH kinematics in the fit to data.

We employ the same neural networks to separate VBF-like signal and background processes as in the ggH analysis, while MELA discriminants offer optimal separation between different signal hypotheses (shown in Table 5). We use $\mathcal{D}_{2\text{jet}}^{\text{VBF}}$, defined in Eq. (15), to separate SM ggH production from the SM VBF production. Several MELA discriminants, as defined in Eq. (20), are constructed to optimally separate the SM hypothesis from the potential anomalous coupling in the VBF production:

$$\begin{aligned} \mathcal{D}_{0-} &= \frac{\mathcal{P}_{\text{SM}}^{\text{VBF}}}{\mathcal{P}_{\text{SM}}^{\text{VBF}} + \mathcal{P}_{0-}^{\text{VBF}}}, & \mathcal{D}_{0h+} &= \frac{\mathcal{P}_{\text{SM}}^{\text{VBF}}}{\mathcal{P}_{\text{SM}}^{\text{VBF}} + \mathcal{P}_{a2}^{\text{VBF}}}, \\ \mathcal{D}_{\Lambda 1} &= \frac{\mathcal{P}_{\text{SM}}^{\text{VBF}}}{\mathcal{P}_{\text{SM}}^{\text{VBF}} + \mathcal{P}_{\Lambda 1}^{\text{VBF}}}, & \mathcal{D}_{\Lambda 1}^{Z\gamma} &= \frac{\mathcal{P}_{\text{SM}}^{\text{VBF}}}{\mathcal{P}_{\text{SM}}^{\text{VBF}} + \mathcal{P}_{\Lambda 1}^{Z\gamma}}. \end{aligned} \quad (20)$$

As for the Hgg analysis, we also define a pure CP -odd MELA discriminant $\mathcal{D}_{CP}^{\text{VBF}}$ in Eq. (21), that is sensitive to interference effects between the SM and pseudoscalar H contributions to directly

probe for CP -violation in the HVV vertex:

$$\mathcal{D}_{CP}^{\text{VBF}} = \frac{\mathcal{P}_{\text{SM}-0-}^{\text{VBF}}}{\mathcal{P}_{\text{SM}}^{\text{VBF}} + \mathcal{P}_{0-}^{\text{VBF}}}. \quad (21)$$

The results of the VBF analysis are extracted with a global maximum likelihood fit based on 4D or 3D, 2D, and 1D distributions built in each of the VBF, boosted, and 0-jet categories, respectively. The templates constructed for the boosted and 0-jet categories are identical to those described for the ggH analysis in Section 9.1, although we note that in this case, in contrast to the former case, the chosen observables do provide some differentiation between anomalous coupling scenarios.

Depending on the anomalous coupling parameter being measured, we use three or four observables in total to construct the distributions in the VBF category. In all cases we include the \mathcal{D}_{NN} and $\mathcal{D}_{2\text{jet}}^{\text{VBF}}$ observables. We additionally include \mathcal{D}_{0-} , \mathcal{D}_{0h+} , $\mathcal{D}_{\Lambda 1}$, or $\mathcal{D}_{\Lambda 1}^{Z\gamma}$, when we measure f_{a3} , f_{a2} , $f_{\Lambda 1}$, or $f_{\Lambda 1}^{Z\gamma}$, respectively; which we will collectively refer to as \mathcal{D}_{BSM} in the following. The fourth observable, which is included only for the measurement of the CP -odd parameter f_{a3} , is $\mathcal{D}_{CP}^{\text{VBF}}$. The selected events are binned into templates constructed using these observables.

The binning of the templates has been optimized following the criteria outlined in Section 9.1. For the $\ell\tau_h$ and $\tau_h\tau_h$ channels, we use 10, 8, and 4 equally sized bins for \mathcal{D}_{BSM} , \mathcal{D}_{NN} , and $\mathcal{D}_{2\text{jet}}^{\text{VBF}}$, respectively. For the $e\mu$ channel, we respectively use 3, 2, and 4 bins for these observables. In all cases, neighboring bins are merged such that the background prediction has no bins with statistical uncertainty larger than 50%. For the measurement of the f_{a3} parameter we include two bins in the $\mathcal{D}_{CP}^{\text{VBF}}$ discriminant, $\mathcal{D}_{CP}^{\text{VBF}} < 0$ and $\mathcal{D}_{CP}^{\text{VBF}} \geq 0$, to bring sensitivity to the sign of the interference between the CP -even and CP -odd contributions. The expected symmetry between these bins is enforced for the background and CP -conserving signal templates to reduce the influence of statistical fluctuations.

10.1 Results of the HVV analysis

The four f_{ai} parameters describing anomalous HVV couplings, as defined in Eqs. (1) and (3), are tested against the data according to the likelihood function defined in Eq. (18), following the same approach as that utilized in the analysis of the Hgg vertex.

An example of a pre-fit distribution in the most sensitive VBF category for the $\tau_h\tau_h$ channel is shown in Fig. 8. The results of the likelihood scans for Approaches 1 and 2 are listed in Table 8 and shown in Figs. 9 and 10, respectively. In each fit, the values of the other anomalous coupling parameters are set to zero, with the exception of the fit to the CP -odd parameter f_{a3} , which is extracted with f_{a3}^{ggH} left unconstrained. The signal strength parameters μ_{qqH} and μ_{ggH} are also profiled for all measurements. The best fit values of these parameters are consistent with unity.

The presence of two minima in the observed likelihood scan for f_{a2} (and to a lesser extent $f_{\Lambda 1}^{Z\gamma}$) is a result of the limited sensitivity to the sign of the interference between the a_1 and a_2 ($\kappa_2^{Z\gamma}$) couplings, which in turn limits the sensitivity to the signs of the f_{a2} ($f_{\Lambda 1}^{Z\gamma}$) parameters.

The CL intervals on f_{ai} at 95% and 68% are more stringent compared to those utilizing the H decay information in the $H \rightarrow 4\ell$ channel [21] because the VBF and VH production processes are sensitive to higher values of q_i^2 appearing in Eq. (1). Therefore, the cross section of anomalous contributions in VBF and VH production increases quickly with f_{ai} . As the cross section

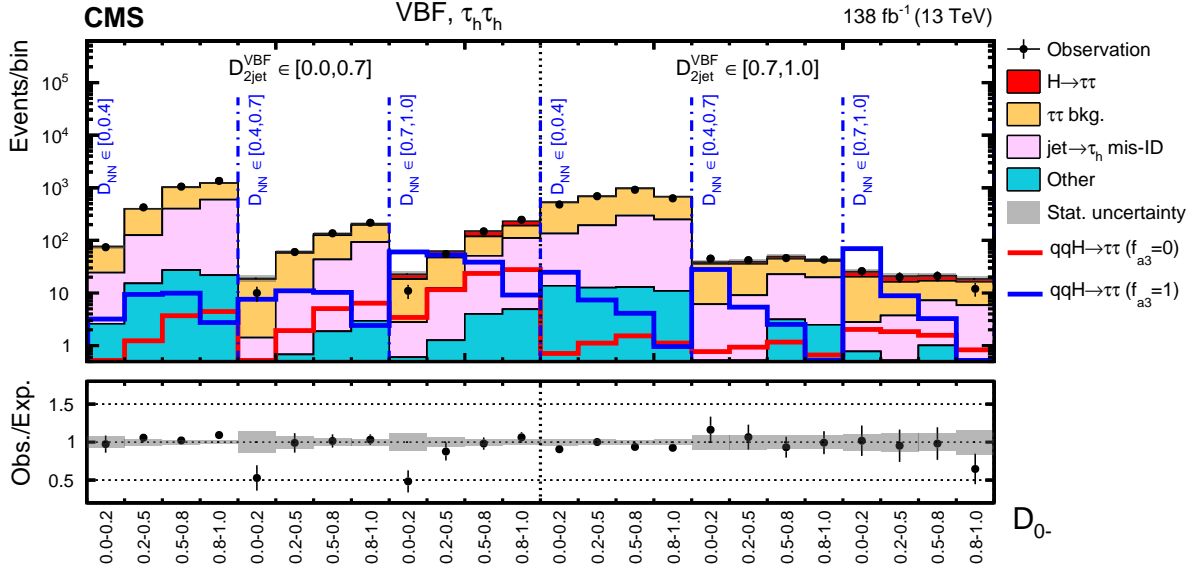


Figure 8: The observed and predicted 3D distribution of $(\mathcal{D}_0, \mathcal{D}_{\text{NN}}, \mathcal{D}_{2\text{jet}}^{\text{VBF}})$ before the fit to data in the $\tau_h \tau_h$ channel for the most sensitive VBF category. The total H signal, including VBF, ggH, and VH processes, is shown stacked on top of the background in the solid red histogram. The VBF+VH signal for the CP-even (CP-odd) scenario is also shown overlaid by the red (blue) line. Only the statistical uncertainties are included in the uncertainty band.

Table 8: Allowed 68% (central values with uncertainties) and 95% CL (in square brackets) intervals on anomalous HVV coupling parameters using the $H \rightarrow \tau\tau$ decay. Approaches 1 and 2 refer to the choice of the relationship between the a_i^{WW} and a_i^{ZZ} couplings, defined in Section 2. For the observed f_{a2} scan, there is a second region allowed at the 68% CL away from the best fit value. We use the union symbol (\cup) to display the additional allowed f_{a2} range in this case.

Approach	Parameter	Observed / (10^{-3})		Expected / (10^{-3})	
		68% CL	95% CL	68% CL	95% CL
Approach 1	f_{a3}	$0.28^{+0.38}_{-0.23}$	$[-0.01, 1.30]$	0.00 ± 0.06	$[-0.23, 0.23]$
	f_{a2}	$1.1^{+0.9}_{-0.9} \cup [-1.8, -0.1]$	$[-3.4, 3.2]$	$0.0^{+0.6}_{-0.5}$	$[-1.4, 1.5]$
	$f_{\Lambda 1}$	$-0.12^{+0.08}_{-0.10}$	$[-0.34, 0.01]$	$0.00^{+0.19}_{-0.05}$	$[-0.15, 0.55]$
	$f_{\Lambda 1}^{Z\gamma}$	2.5 ± 1.8	$[-3.6, 6.6]$	$0.0^{+1.5}_{-1.2}$	$[-3.2, 3.4]$
Approach 2	f_{a3}	$0.40^{+0.53}_{-0.33}$	$[-0.01, 1.90]$	0.00 ± 0.08	$[-0.33, 0.33]$

increases with respect to f_{ai} at different rates for production and decay, relatively small values of f_{ai} correspond to a substantial anomalous contribution to the production cross section. This leads to the plateau in the $-2 \ln \mathcal{L}$ distributions for larger values of f_{ai} in Fig. 9. By using the cross section ratios for VBF production in the f_{ai} definition in Eq. (3), the appearance of the plateau and the narrow exclusion range would change. The f_{ai} constraints in Ref. [21] also utilize the VBF and VH production information, but the number of reconstructed $H \rightarrow 4\ell$ events in these production modes is still low compared to this analysis.

11 Combination of the results with other decay channels

The results of the anomalous coupling measurements presented in the previous sections can be further improved by combining with other H production and decay channels. The precision of

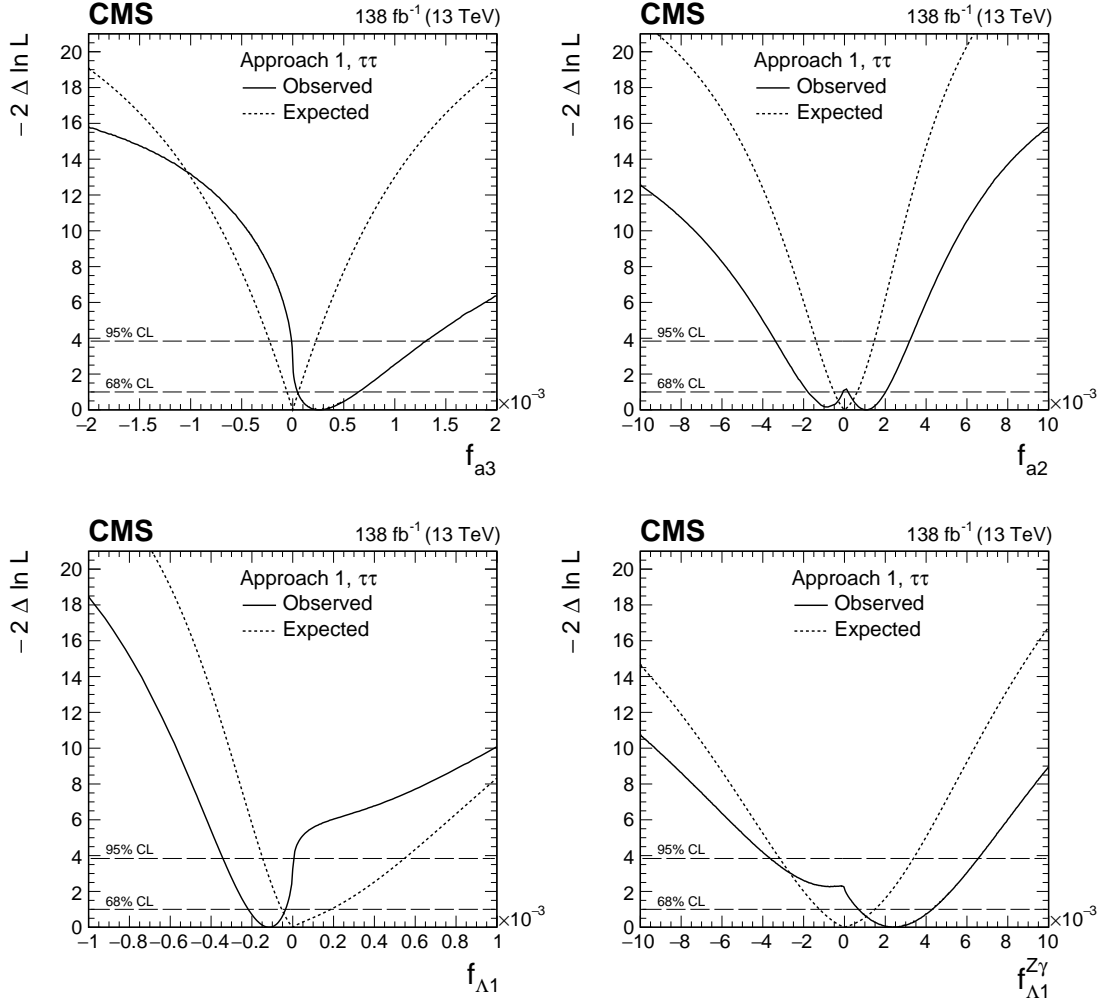


Figure 9: Observed (solid) and expected (dashed) likelihood scans of f_{a3} (upper left), f_{a2} (upper right), $f_{\Lambda 1}$ (lower left), and $f_{\Lambda 1}^{Z\gamma}$ (lower right) in Approach 1 ($a_i^{WW} = a_i^{ZZ}$).

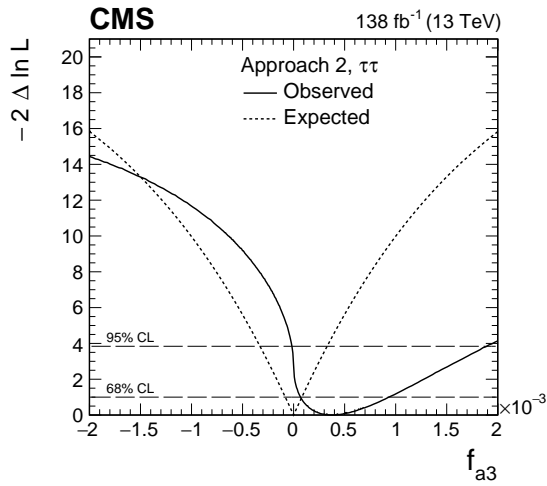


Figure 10: Observed (solid) and expected (dashed) likelihood scans of f_{a3} in Approach 2.

the anomalous HVV and Hgg coupling measurements is improved by combining the $H \rightarrow \tau\tau$ and $H \rightarrow 4\ell$ decay channels, where we consider H production via VBF, VH, and ggH. We additionally constrain the anomalous Htt couplings by combining the $ggH \rightarrow \tau\tau/4\ell$ and $t\bar{t}H/tH \rightarrow \gamma\gamma/4\ell$ channels.

For all combinations, each H decay channel treats anomalous couplings in H production processes in the likelihood in a consistent manner. As with the $H \rightarrow \tau\tau$ only fits, in the likelihood fit for a given parameter the values of the other anomalous couplings are set to zero with the exception of the fits to f_{a3} and f_{a3}^{ggH} , and the signal strength parameters are profiled in the combined likelihood fit. The number of signal strength parameters in the combined fit can be reduced by using a relationship between the production cross section ratios. For example, there are in principle four signal strength parameters for the combination of the $H \rightarrow \tau\tau$ and $H \rightarrow 4\ell$ channels ($\mu_{qqH}^{\tau\tau}, \mu_{ggH}^{\tau\tau}, \mu_{qqH}^{ZZ}, \mu_{ggH}^{ZZ}$). However, one degree of freedom is removed because the ratio between the ggH and VBF+VH cross sections is the same in both channels, $\mu_{qqH}^{\tau\tau}/\mu_{ggH}^{\tau\tau} = \mu_{qqH}^{ZZ}/\mu_{ggH}^{ZZ}$. Therefore, we can parameterize the combined fit with three signal strength parameters μ_{qqH}, μ_{ggH} , and η_τ , where η_τ stands for the relative strength of the H coupling to the τ leptons. For the combination with the $t\bar{t}H$ and tH results using the $H \rightarrow 4\ell$ and $H \rightarrow \gamma\gamma$ channels, the signal strengths $\mu_{t\bar{t}H}^{ZZ}$ and $\mu_{t\bar{t}H}^{\gamma\gamma}$ are not related for the f_{CP}^{Htt} measurement because they could differ by the loop involved in the $H \rightarrow \gamma\gamma$ decay. In the EFT approach, the fully-resolved loop parameterization following Ref. [46] is used to correlate them. All common systematic uncertainties are treated as being correlated between the channels in the combined likelihood fit.

The measurements of anomalous Hgg and HVV couplings using the MELA method are combined with the results using the on-shell $H \rightarrow 4\ell$ decay [21]. In the $H \rightarrow 4\ell$ analysis, anomalous HVV couplings can affect both production (VBF+VH) and decay ($H \rightarrow VV \rightarrow 4\ell$) processes. Information from both processes is taken into account in the analysis. The combination improves the limits on the anomalous coupling parameters typically by about 20–50%.

The combined likelihood scans for the HVV anomalous coupling measurements are shown in Figs. 11–12, and the allowed 68 and 95% CL intervals are listed in Table 9. The $H \rightarrow \tau\tau$ channel results mainly constrain small values of f_{ai} where the H production information is the dominant factor, whereas the $H \rightarrow 4\ell$ analysis provides major constraints at large values of f_{ai} based on the decay information.

Table 9: Allowed 68% (central values with uncertainties) and 95% CL (in square brackets) intervals on anomalous HVV coupling parameters using the $H \rightarrow \tau\tau$ and $H \rightarrow 4\ell$ [21] decay channels, using two approaches described in Section 2 that define the relationship between the a_i^{WW} and a_i^{ZZ} couplings.

Approach	Parameter	Observed/(10^{-3})		Expected/(10^{-3})	
		68% CL	95% CL	68% CL	95% CL
Approach 1	f_{a3}	$0.20^{+0.26}_{-0.16}$	$[-0.01, 0.88]$	0.00 ± 0.05	$[-0.21, 0.21]$
	f_{a2}	$0.7^{+0.8}_{-0.6}$	$[-1.0, 2.5]$	$0.0^{+0.5}_{-0.4}$	$[-1.1, 1.2]$
	$f_{\Delta 1}$	$-0.04^{+0.04}_{-0.08}$	$[-0.22, 0.16]$	$0.00^{+0.11}_{-0.04}$	$[-0.11, 0.38]$
	$f_{\Delta 1}^{Z\gamma}$	$0.7^{+1.6}_{-1.3}$	$[-2.7, 4.1]$	$0.0^{+1.0}_{-1.0}$	$[-2.6, 2.5]$
Approach 2	f_{a3}	$0.28^{+0.39}_{-0.23}$	$[-0.01, 1.28]$	0.00 ± 0.08	$[-0.30, 0.30]$

The combined likelihood scans for the Hgg anomalous coupling measurements are shown in Fig. 13, and the allowed 68 and 95% CL intervals are listed in Table 10. The $H \rightarrow \tau\tau$ channel is

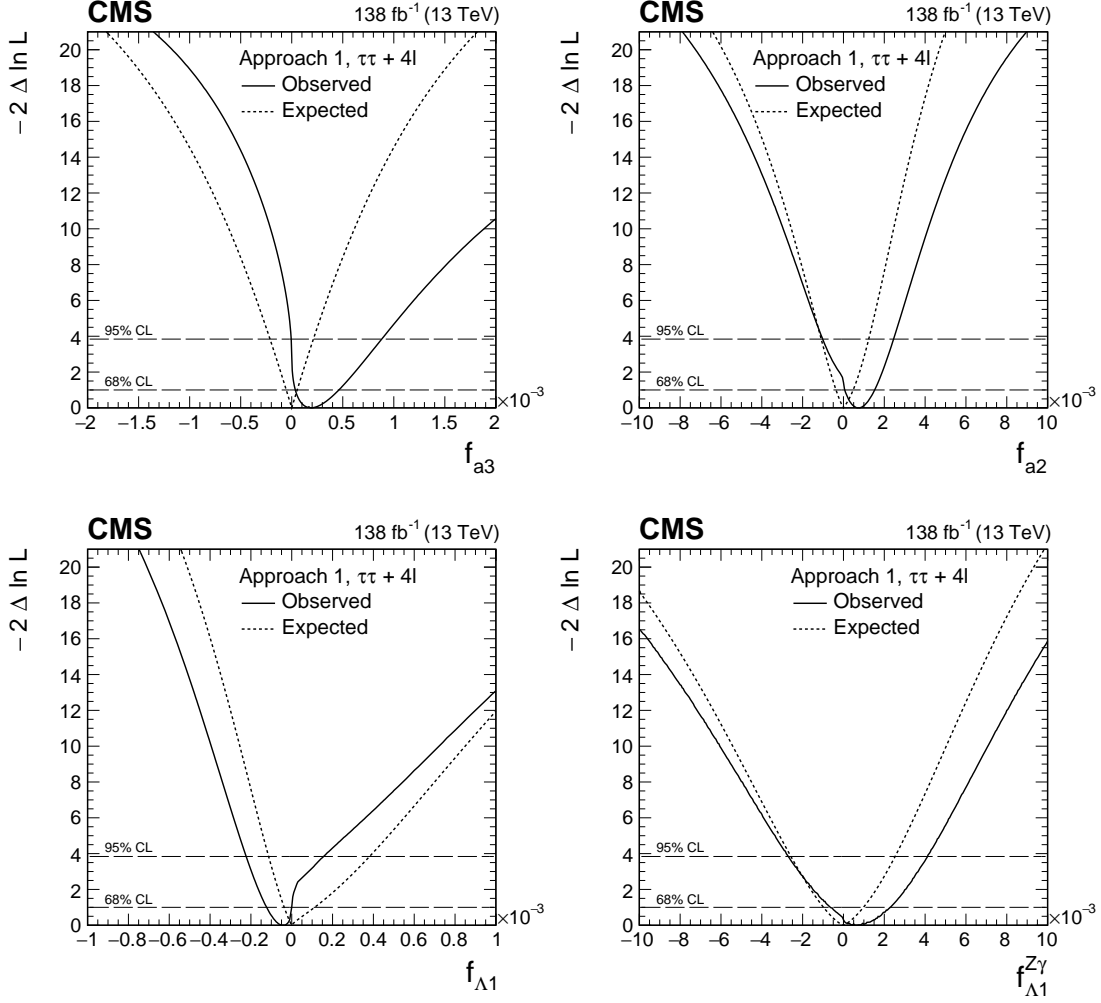


Figure 11: Observed (solid) and expected (dashed) likelihood scans of f_{a3} (upper left), f_{a2} (upper right), $f_{\Lambda 1}$ (lower left), and $f_{\Lambda 1}^{Z\gamma}$ (lower right) in Approach 1 ($a_i^{WW} = a_i^{ZZ}$) obtained with the combination of results using the $H \rightarrow \tau\tau$ and $H \rightarrow 4\ell$ [21] decay channels.

more sensitive to f_{a3}^{ggH} than the $H \rightarrow 4\ell$ channel is, but there is a significant improvement from including both channels in the combination. Previous measurements by the CMS and ATLAS Collaborations [21, 31] were only able to differentiate between the CP -even and CP -odd scenarios with a significance slightly less than 1 standard deviation. With the current measurement, the pure CP -odd scenario is excluded with a observed (expected) significance of 2.4 standard deviations (1.8 standard deviations), which is cross-checked with pseudo-experiments.

Constraints on anomalous $H\tau\tau$ couplings are obtained through the combination of the Hgg results with measurements of the $t\bar{t}H$ and tH processes in the $H \rightarrow 4\ell$ [21] and $H \rightarrow \gamma\gamma$ [20] channels. We measure the $f_{CP}^{H\tau\tau}$ parameter by relating f_{a3}^{ggH} and $f_{CP}^{H\tau\tau}$ as described in Eq. (10), under the assumption of top quark dominance in the ggH loop. The results are presented in Fig. 13 and Table 10.

The combination of Hgg , $t\bar{t}H$, and tH results can be reinterpreted in the EFT approach as constraints on c_{gg} and \tilde{c}_{gg} . The likelihood scans for c_{gg} and \tilde{c}_{gg} are performed with κ_t and $\tilde{\kappa}_t$ either profiled or fixed to SM expectation ($\kappa_t = 1$, $\tilde{\kappa}_t = 0$). The reinterpretation is presented in Fig. 14 and Table 11. We note that in both c_{gg} scans there is a second minimum away from

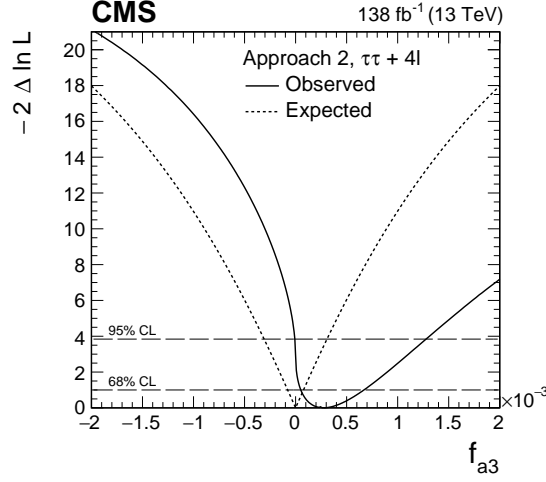


Figure 12: Observed (solid) and expected (dashed) likelihood scans of f_{a3} in Approach 2 (defined in Section 2) obtained with the combination of results using the $H \rightarrow \tau\tau$ and $H \rightarrow 4\ell$ [21] decay channels.

Table 10: Allowed 68% (central values with uncertainties) and 95% CL (in square brackets) intervals on f_{a3}^{ggH} , from the combination of the $H \rightarrow \tau\tau$ and $H \rightarrow 4\ell$ [21] decay channels, and f_{CP}^{Htt} , from the combination of the $H \rightarrow \tau\tau$, $H \rightarrow 4\ell$ [21], and $H \rightarrow \gamma\gamma$ [20] decay channels.

Parameter	Observed		Expected	
	68% CL	95% CL	68% CL	95% CL
f_{a3}^{ggH}	$0.07^{+0.32}_{-0.07}$	$[-0.15, 0.89]$	0.00 ± 0.26	—
f_{CP}^{Htt}	$0.03^{+0.17}_{-0.03}$	$[-0.07, 0.51]$	0.00 ± 0.12	$[-0.49, 0.49]$

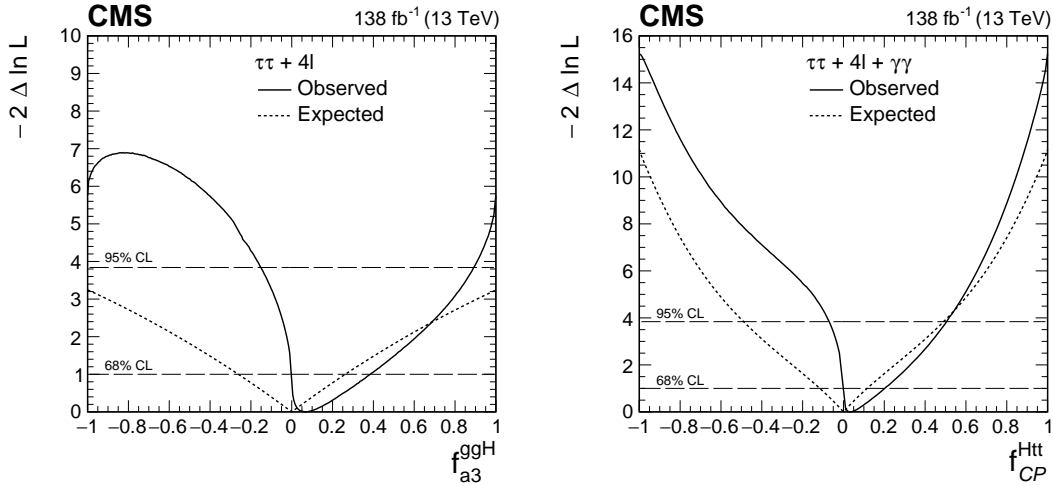


Figure 13: Left: the observed (solid) and expected (dashed) likelihood scans of f_{a3}^{ggH} obtained with the combination of results using the $H \rightarrow \tau\tau$ and $H \rightarrow 4\ell$ [21] decay channels. Right: The observed (solid) and expected (dashed) likelihood scans of f_{CP}^{Htt} obtained with the combination of results using the $H \rightarrow \tau\tau$, $H \rightarrow 4\ell$ [21], and $H \rightarrow \gamma\gamma$ [20] decay channels.

$c_{gg} = 0$ due to the negative interference between the c_{gg} and κ_t contributions, as follows from Eq. (8). The value of the $-2\Delta \ln \mathcal{L}$ at c_{gg} between the two minima points is larger for the

observed scan compared to the expected, due to the statistical fluctuation in the $H \rightarrow \tau\tau$ channel data described in Section 9.3.

Table 11: Allowed 68% (central values with uncertainties) and 95% CL (in square brackets) intervals on c_{gg} and \tilde{c}_{gg} using the $H \rightarrow \tau\tau$, $H \rightarrow 4\ell$ [21], and $H \rightarrow \gamma\gamma$ [20] decay channels. Results are presented for two scenarios: κ_t and $\tilde{\kappa}_t$ profiled in the fit, and κ_t and $\tilde{\kappa}_t$ fixed to the SM expectation. In instances where there is a second allowed region away from the best fit value at a given CL, we use the union symbol (\cup) to display the additional allowed \tilde{c}_{gg}/c_{gg} range.

Parameter	Scenario		68% CL / (10^{-2})	95% CL / (10^{-2})
c_{gg}	Profiled	Observed	$-0.11^{+0.20}_{-0.26} \cup [-1.85, -1.42]$	$[-2.12, -1.35] \cup [-0.71, 0.36]$
		Expected	$0.00^{+0.18}_{-0.27} \cup [-1.91, -1.48]$	$[-2.23, 0.37]$
\tilde{c}_{gg}	Profiled	Observed	0.00 ± 1.29	$[-1.79, 1.79]$
		Expected	0.00 ± 1.15	$[-1.78, 1.78]$
c_{gg}	Fixed	Observed	$-0.08^{+0.07}_{-0.15} \cup [-1.65, -1.54]$	$[-1.71, -1.54] \cup [-0.59, 0.05]$
		Expected	$0.00^{+0.06}_{-0.14} \cup [-1.73, -1.50]$	$[-1.78, 0.12]$
\tilde{c}_{gg}	Fixed	Observed	$0.22^{+0.28}_{-0.22} \cup [-0.50, 0.00]$	$[-0.74, 0.75]$
		Expected	0.00 ± 0.45	$[-0.87, 0.87]$

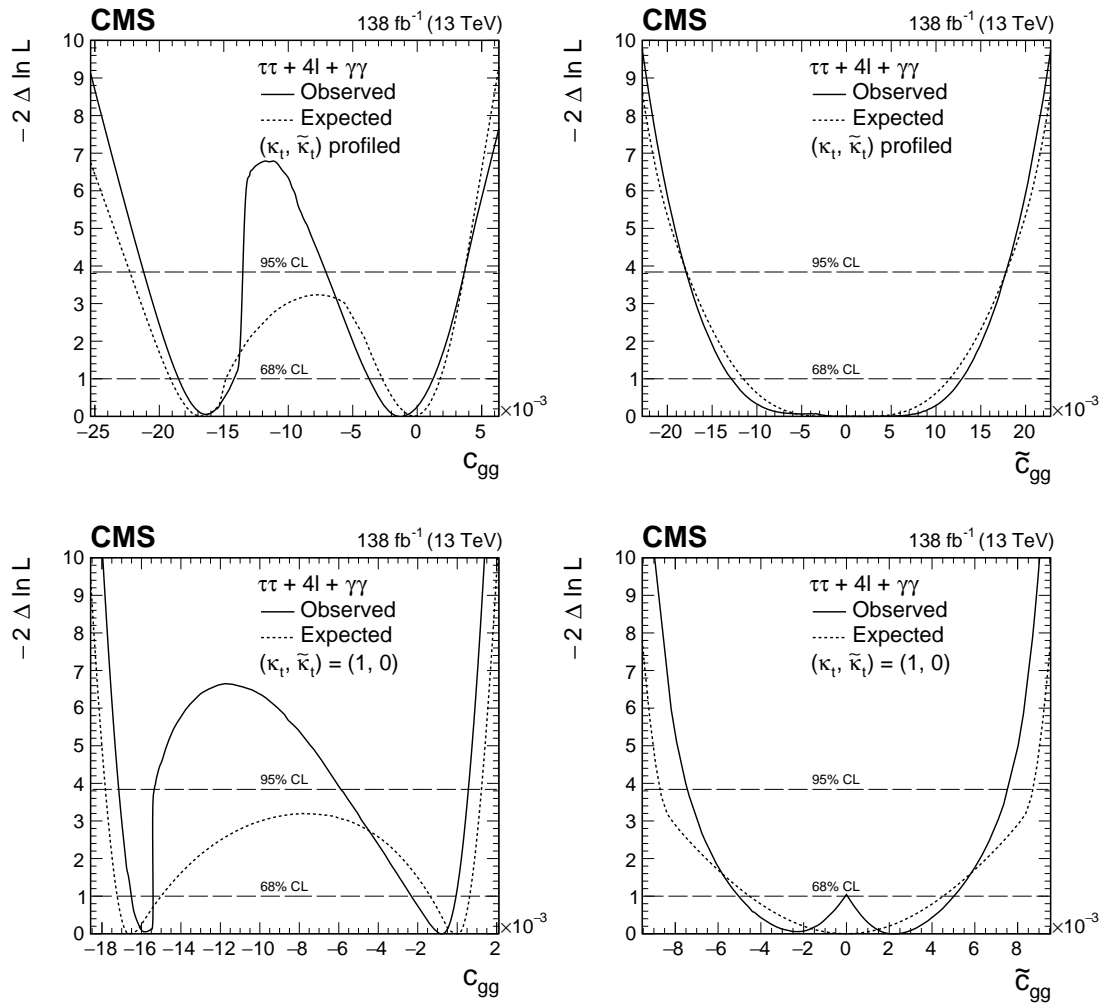


Figure 14: Observed (solid) and expected (dashed) likelihood scans of c_{gg} (left) and \tilde{c}_{gg} (right) with κ_t and $\tilde{\kappa}_t$ profiled (upper) and fixed to SM expectation (lower) using the $H \rightarrow \tau\tau$, $H \rightarrow 4\ell$ [21], and $H \rightarrow \gamma\gamma$ [20] decay channels.

12 Summary

A study is presented of anomalous interactions of the Higgs boson (H) with vector bosons, including CP violation, using its associated production with two hadronic jets in gluon fusion (ggH), vector boson fusion (VBF), and associated production with a vector boson, and a subsequent decay to a pair of τ leptons. Constraints have been set on the CP -violating effects in ggH production in terms of the effective cross section ratio f_{a3}^{ggH} , or equivalently the effective mixing angle α^{Hff} , using matrix element techniques. The ggH production analysis results in the most stringent limits on CP violation in ggH production to date. In the VBF production analysis, constraints on the CP -violating parameter f_{a3} and on the CP -conserving parameters f_{a2} , $f_{\Lambda 1}$, and $f_{\Lambda 1}^{Z\gamma}$ have been set using matrix element techniques. Further constraints were obtained in the combination of the $H \rightarrow \tau\tau$, $H \rightarrow 4\ell$, and $H \rightarrow \gamma\gamma$ channels. The combination improves the limits on the anomalous coupling parameters typically by about 20–50%. The analysis excludes the pure CP -odd scenario of the Higgs coupling to gluons with a significance of 2.4 standard deviations.

References

- [1] ATLAS Collaboration, “Observation of a new particle in the search for the standard model Higgs boson with the ATLAS detector at the LHC”, *Phys. Lett. B* **716** (2012) 1, doi:10.1016/j.physletb.2012.08.020, arXiv:1207.7214.
- [2] CMS Collaboration, “Observation of a new boson at a mass of 125 GeV with the CMS experiment at the LHC”, *Phys. Lett. B* **716** (2012) 30, doi:10.1016/j.physletb.2012.08.021, arXiv:1207.7235.
- [3] CMS Collaboration, “Observation of a new boson with mass near 125 GeV in pp collisions at $\sqrt{s} = 7$ and 8 TeV”, *JHEP* **06** (2013) 081, doi:10.1007/JHEP06(2013)081, arXiv:1303.4571.
- [4] S. L. Glashow, “Partial-symmetries of weak interactions”, *Nucl. Phys.* **22** (1961) 579, doi:10.1016/0029-5582(61)90469-2.
- [5] F. Englert and R. Brout, “Broken symmetry and the mass of gauge vector mesons”, *Phys. Rev. Lett.* **13** (1964) 321, doi:10.1103/PhysRevLett.13.321.
- [6] P. W. Higgs, “Broken symmetries, massless particles and gauge fields”, *Phys. Lett.* **12** (1964) 132, doi:10.1016/0031-9163(64)91136-9.
- [7] P. W. Higgs, “Broken symmetries and the masses of gauge bosons”, *Phys. Rev. Lett.* **13** (1964) 508, doi:10.1103/PhysRevLett.13.508.
- [8] G. S. Guralnik, C. R. Hagen, and T. W. B. Kibble, “Global conservation laws and massless particles”, *Phys. Rev. Lett.* **13** (1964) 585, doi:10.1103/PhysRevLett.13.585.
- [9] S. Weinberg, “A model of leptons”, *Phys. Rev. Lett.* **19** (1967) 1264, doi:10.1103/PhysRevLett.19.1264.
- [10] A. Salam, “Weak and electromagnetic interactions”, *Conf. Proc. C* **680519** (1968) 367, doi:10.1142/9789812795915_0034.
- [11] CMS Collaboration, “Constraints on the spin-parity and anomalous HVV couplings of the Higgs boson in proton collisions at 7 and 8 TeV”, *Phys. Rev. D* **92** (2015) 012004, doi:10.1103/PhysRevD.92.012004, arXiv:1411.3441.

- [12] ATLAS Collaboration, “Study of the spin and parity of the Higgs boson in diboson decays with the ATLAS detector”, *Eur. Phys. J. C* **75** (2015) 476, doi:10.1140/epjc/s10052-015-3685-1, arXiv:1506.05669.
- [13] CMS Collaboration, “Study of the mass and spin-parity of the Higgs boson candidate via its decays to Z boson pairs”, *Phys. Rev. Lett.* **110** (2013) 081803, doi:10.1103/PhysRevLett.110.081803, arXiv:1212.6639.
- [14] CMS Collaboration, “Measurement of the properties of a Higgs boson in the four-lepton final state”, *Phys. Rev. D* **89** (2014) 092007, doi:10.1103/PhysRevD.89.092007, arXiv:1312.5353.
- [15] CMS Collaboration, “Limits on the Higgs boson lifetime and width from its decay to four charged leptons”, *Phys. Rev. D* **92** (2015) 072010, doi:10.1103/PhysRevD.92.072010, arXiv:1507.06656.
- [16] CMS Collaboration, “Combined search for anomalous pseudoscalar HVV couplings in $VH(H \rightarrow b\bar{b})$ production and $H \rightarrow VV$ decay”, *Phys. Lett. B* **759** (2016) 672, doi:10.1016/j.physletb.2016.06.004, arXiv:1602.04305.
- [17] CMS Collaboration, “Constraints on anomalous Higgs boson couplings using production and decay information in the four-lepton final state”, *Phys. Lett. B* **775** (2017) 1, doi:10.1016/j.physletb.2017.10.021, arXiv:1707.00541.
- [18] CMS Collaboration, “Measurements of the Higgs boson width and anomalous HVV couplings from on-shell and off-shell production in the four-lepton final state”, *Phys. Rev. D* **99** (2019) 112003, doi:10.1103/PhysRevD.99.112003, arXiv:1901.00174.
- [19] CMS Collaboration, “Constraints on anomalous HVV couplings from the production of Higgs bosons decaying to τ lepton pairs”, *Phys. Rev. D* **100** (2019) 112002, doi:10.1103/PhysRevD.100.112002, arXiv:1903.06973.
- [20] CMS Collaboration, “Measurements of $t\bar{t}H$ production and the CP structure of the Yukawa interaction between the Higgs boson and top quark in the diphoton decay channel”, *Phys. Rev. Lett.* **125** (2020) 061801, doi:10.1103/PhysRevLett.125.061801, arXiv:2003.10866.
- [21] CMS Collaboration, “Constraints on anomalous Higgs boson couplings to vector bosons and fermions in its production and decay using the four-lepton final state”, *Phys. Rev. D* **104** (2021) 052004, doi:10.1103/PhysRevD.104.052004, arXiv:2104.12152.
- [22] CMS Collaboration, “Analysis of the CP structure of the Yukawa coupling between the Higgs boson and τ leptons in proton-proton collisions at $\sqrt{s} = 13$ TeV”, 2021. arXiv:2110.04836. Submitted to *JHEP*.
- [23] CMS Collaboration, “First evidence for off-shell production of the Higgs boson and measurement of its width”, 2022. arXiv:2202.06923. Submitted to *Nature Physics*.
- [24] ATLAS Collaboration, “Evidence for the spin-0 nature of the Higgs boson using ATLAS data”, *Phys. Lett. B* **726** (2013) 120, doi:10.1016/j.physletb.2013.08.026, arXiv:1307.1432.

-
- [25] ATLAS Collaboration, “Test of CP invariance in vector-boson fusion production of the Higgs boson using the optimal observable method in the ditau decay channel with the ATLAS detector”, *Eur. Phys. J. C* **76** (2016) 658, doi:10.1140/epjc/s10052-016-4499-5, arXiv:1602.04516.
 - [26] ATLAS Collaboration, “Measurement of inclusive and differential cross sections in the $H \rightarrow ZZ^* \rightarrow 4\ell$ decay channel in pp collisions at $\sqrt{s} = 13$ TeV with the ATLAS detector”, *JHEP* **10** (2017) 132, doi:10.1007/JHEP10(2017)132, arXiv:1708.02810.
 - [27] ATLAS Collaboration, “Measurement of the Higgs boson coupling properties in the $H \rightarrow ZZ^* \rightarrow 4\ell$ decay channel at $\sqrt{s} = 13$ TeV with the ATLAS detector”, *JHEP* **03** (2018) 095, doi:10.1007/JHEP03(2018)095, arXiv:1712.02304.
 - [28] ATLAS Collaboration, “Measurements of Higgs boson properties in the diphoton decay channel with 36 fb^{-1} of pp collision data at $\sqrt{s} = 13$ TeV with the ATLAS detector”, *Phys. Rev. D* **98** (2018) 052005, doi:10.1103/PhysRevD.98.052005, arXiv:1802.04146.
 - [29] ATLAS Collaboration, “Test of CP invariance in vector-boson fusion production of the Higgs boson in the $H \rightarrow \tau\tau$ channel in proton–proton collisions at $\sqrt{s} = 13$ TeV with the ATLAS detector”, *Phys. Lett. B* **805** (2020) 135426, doi:10.1016/j.physletb.2020.135426, arXiv:2002.05315.
 - [30] ATLAS Collaboration, “CP properties of Higgs boson interactions with top quarks in the $t\bar{t}H$ and tH processes using $H \rightarrow \gamma\gamma$ with the ATLAS detector”, *Phys. Rev. Lett.* **125** (2020) 061802, doi:10.1103/PhysRevLett.125.061802, arXiv:2004.04545.
 - [31] ATLAS Collaboration, “Constraints on Higgs boson properties using $WW^*(\rightarrow e\nu\mu\nu)jj$ production in 36.1 fb^{-1} of $\sqrt{s} = 13$ TeV pp collisions with the ATLAS detector”, 2021. arXiv:2109.13808. Submitted to *Eur. Phys. J. C*.
 - [32] Y. Gao et al., “Spin determination of single-produced resonances at hadron colliders”, *Phys. Rev. D* **81** (2010) 075022, doi:10.1103/PhysRevD.81.075022, arXiv:1001.3396.
 - [33] S. Bolognesi et al., “Spin and parity of a single-produced resonance at the LHC”, *Phys. Rev. D* **86** (2012) 095031, doi:10.1103/PhysRevD.86.095031, arXiv:1208.4018.
 - [34] I. Anderson et al., “Constraining anomalous HVV interactions at proton and lepton colliders”, *Phys. Rev. D* **89** (2014) 035007, doi:10.1103/PhysRevD.89.035007, arXiv:1309.4819.
 - [35] A. V. Gritsan, R. Röntsch, M. Schulze, and M. Xiao, “Constraining anomalous Higgs boson couplings to the heavy flavor fermions using matrix element techniques”, *Phys. Rev. D* **94** (2016) 055023, doi:10.1103/PhysRevD.94.055023, arXiv:1606.03107.
 - [36] HEPData record for this analysis, 2022. doi:10.17182/hepdata.129530.
 - [37] T. Plehn, D. L. Rainwater, and D. Zeppenfeld, “Determining the structure of Higgs couplings at the LHC”, *Phys. Rev. Lett.* **88** (2002) 051801, doi:10.1103/PhysRevLett.88.051801, arXiv:hep-ph/0105325.
 - [38] V. Hankele, G. Klamke, D. Zeppenfeld, and T. Figy, “Anomalous Higgs boson couplings in vector boson fusion at the CERN LHC”, *Phys. Rev. D* **74** (2006) 095001, doi:10.1103/PhysRevD.74.095001, arXiv:hep-ph/0609075.

- [39] E. Accomando et al., “Workshop on CP studies and non-standard Higgs physics”, 2006. arXiv:hep-ph/0608079.
- [40] K. Hagiwara, Q. Li, and K. Mawatari, “Jet angular correlation in vector-boson fusion processes at hadron colliders”, *JHEP* **07** (2009) 101, doi:10.1088/1126-6708/2009/07/101, arXiv:0905.4314.
- [41] A. De Rújula et al., “Higgs look-alikes at the LHC”, *Phys. Rev. D* **82** (2010) 013003, doi:10.1103/PhysRevD.82.013003, arXiv:1001.5300.
- [42] J. Ellis, D. S. Hwang, V. Sanz, and T. You, “A fast track towards the ‘Higgs’ spin and parity”, *JHEP* **11** (2012) 134, doi:10.1007/JHEP11(2012)134, arXiv:1208.6002.
- [43] P. Artoisenet et al., “A framework for Higgs characterisation”, *JHEP* **11** (2013) 043, doi:10.1007/JHEP11(2013)043, arXiv:1306.6464.
- [44] M. J. Dolan, P. Harris, M. Jankowiak, and M. Spannowsky, “Constraining CP-violating Higgs sectors at the LHC using gluon fusion”, *Phys. Rev. D* **90** (2014) 073008, doi:10.1103/PhysRevD.90.073008, arXiv:1406.3322.
- [45] A. Greljo, G. Isidori, J. M. Lindert, and D. Marzocca, “Pseudo-observables in electroweak Higgs production”, *Eur. Phys. J. C* **76** (2016) 158, doi:10.1140/epjc/s10052-016-4000-5, arXiv:1512.06135.
- [46] J. Davis et al., “Constraining anomalous Higgs boson couplings to virtual photons”, 2021. arXiv:2109.13363.
- [47] A. V. Gritsan et al., “New features in the JHU generator framework: constraining Higgs boson properties from on-shell and off-shell production”, *Phys. Rev. D* **102** (2020) 056022, doi:10.1103/PhysRevD.102.056022, arXiv:2002.09888.
- [48] LHC Higgs Cross Section Working Group, “Handbook of LHC Higgs cross sections: 4. deciphering the nature of the Higgs sector”, *CERN* (2016) doi:10.23731/CYRM-2017-002, arXiv:1610.07922.
- [49] K. Hamilton, P. Nason, and G. Zanderighi, “Finite quark-mass effects in the NNLOPS POWHEG+MiNLO Higgs generator”, *JHEP* **05** (2015) 140, doi:10.1007/JHEP05(2015)140, arXiv:1501.04637.
- [50] G. Klamke and D. Zeppenfeld, “Higgs plus two jet production via gluon fusion as a signal at the CERN LHC”, *JHEP* **04** (2007) 052, doi:10.1088/1126-6708/2007/04/052, arXiv:hep-ph/0703202.
- [51] V. Hankele, G. Klamke, and D. Zeppenfeld, “Higgs + 2 jets as a probe for CP properties”, 2006. arXiv:hep-ph/0605117.
- [52] CMS Collaboration, “The CMS trigger system”, *JINST* **12** (2017) P01020, doi:10.1088/1748-0221/12/01/P01020, arXiv:1609.02366.
- [53] CMS Collaboration, “The CMS experiment at the CERN LHC”, *JINST* **3** (2008) S08004, doi:10.1088/1748-0221/3/08/S08004.
- [54] CMS Collaboration, “Precision luminosity measurement in proton-proton collisions at $\sqrt{s} = 13$ TeV in 2015 and 2016 at CMS”, *Eur. Phys. J. C* **81** (2021) 800, doi:10.1140/epjc/s10052-021-09538-2, arXiv:2104.01927.

-
- [55] CMS Collaboration, “CMS luminosity measurement for the 2017 data-taking period at $\sqrt{s} = 13$ TeV”, CMS Physics Analysis Summary CMS-PAS-LUM-17-004, 2018.
- [56] CMS Collaboration, “CMS luminosity measurement for the 2018 data-taking period at $\sqrt{s} = 13$ TeV”, CMS Physics Analysis Summary CMS-PAS-LUM-18-002, 2019.
- [57] T. Sjöstrand et al., “An introduction to PYTHIA 8.2”, *Comput. Phys. Commun.* **191** (2015) 159, doi:10.1016/j.cpc.2015.01.024, arXiv:1410.3012.
- [58] GEANT4 Collaboration, “GEANT4—a simulation toolkit”, *Nucl. Instrum. Meth. A* **506** (2003) 250, doi:10.1016/S0168-9002(03)01368-8.
- [59] P. Nason, “A new method for combining NLO QCD with shower Monte Carlo algorithms”, *JHEP* **11** (2004) 040, doi:10.1088/1126-6708/2004/11/040, arXiv:hep-ph/0409146.
- [60] S. Frixione, P. Nason, and C. Oleari, “Matching NLO QCD computations with parton shower simulations: the POWHEG method”, *JHEP* **11** (2007) 070, doi:10.1088/1126-6708/2007/11/070, arXiv:0709.2092.
- [61] S. Alioli, P. Nason, C. Oleari, and E. Re, “A general framework for implementing NLO calculations in shower Monte Carlo programs: the POWHEG BOX”, *JHEP* **06** (2010) 043, doi:10.1007/JHEP06(2010)043, arXiv:1002.2581.
- [62] P. Nason and C. Oleari, “NLO Higgs boson production via vector-boson fusion matched with shower in POWHEG”, *JHEP* **02** (2010) 037, doi:10.1007/JHEP02(2010)037, arXiv:0911.5299.
- [63] T. Ježo and P. Nason, “On the treatment of resonances in next-to-leading order calculations matched to a parton shower”, *JHEP* **12** (2015) 065, doi:10.1007/JHEP12(2015)065, arXiv:1509.09071.
- [64] F. Granata, J. M. Lindert, C. Oleari, and S. Pozzorini, “NLO QCD+EW predictions for HV and HV+jet production including parton-shower effects”, *JHEP* **09** (2017) 012, doi:10.1007/JHEP09(2017)012, arXiv:1706.03522.
- [65] J. Alwall et al., “The automated computation of tree-level and next-to-leading order differential cross sections, and their matching to parton shower simulations”, *JHEP* **07** (2014) 079, doi:10.1007/JHEP07(2014)079, arXiv:1405.0301.
- [66] R. Frederix and S. Frixione, “Merging meets matching in MC@NLO”, *JHEP* **12** (2012) 061, doi:10.1007/JHEP12(2012)061, arXiv:1209.6215.
- [67] F. Demartin et al., “Higgs characterisation at NLO in QCD: CP properties of the top-quark Yukawa interaction”, *Eur. Phys. J. C* **74** (2014) 3065, doi:10.1140/epjc/s10052-014-3065-2, arXiv:1407.5089.
- [68] K. Hamilton, P. Nason, E. Re, and G. Zanderighi, “NNLOPS simulation of Higgs boson production”, *JHEP* **10** (2013) 222, doi:10.1007/JHEP10(2013)222, arXiv:1309.0017.
- [69] S. Alioli, S.-O. Moch, and P. Uwer, “Hadronic top-quark pair-production with one jet and parton showering”, *JHEP* **01** (2012) 137, doi:10.1007/JHEP01(2012)137, arXiv:1110.5251.

- [70] R. Frederix, E. Re, and P. Torrielli, “Single-top t -channel hadroproduction in the four-flavour scheme with POWHEG and aMC@NLO”, *JHEP* **09** (2012) 130, doi:10.1007/JHEP09(2012)130, arXiv:1207.5391.
- [71] E. Re, “Single-top Wt-channel production matched with parton showers using the POWHEG method”, *Eur. Phys. J. C* **71** (2011) 1547, doi:10.1140/epjc/s10052-011-1547-z, arXiv:1009.2450.
- [72] J. Alwall et al., “Comparative study of various algorithms for the merging of parton showers and matrix elements in hadronic collisions”, *Eur. Phys. J. C* **53** (2008) 473, doi:10.1140/epjc/s10052-007-0490-5, arXiv:0706.2569.
- [73] CMS Collaboration, “Event generator tunes obtained from underlying event and multiparton scattering measurements”, *Eur. Phys. J. C* **76** (2016) 155, doi:10.1140/epjc/s10052-016-3988-x, arXiv:1512.00815.
- [74] CMS Collaboration, “Investigations of the impact of the parton shower tuning in Pythia 8 in the modelling of $t\bar{t}$ at $\sqrt{s} = 8$ and 13 TeV”, CMS Physics Analysis Summary CMS-PAS-TOP-16-021, 2016.
- [75] CMS Collaboration, “Extraction and validation of a new set of CMS PYTHIA8 tunes from underlying-event measurements”, *Eur. Phys. J. C* **80** (2020) 4, doi:10.1140/epjc/s10052-019-7499-4, arXiv:1903.12179.
- [76] NNPDF Collaboration, “Parton distributions for the LHC Run II”, *JHEP* **04** (2015) 040, doi:10.1007/JHEP04(2015)040, arXiv:1410.8849.
- [77] NNPDF Collaboration, “Parton distributions from high-precision collider data”, *Eur. Phys. J. C* **77** (2017) 663, doi:10.1140/epjc/s10052-017-5199-5, arXiv:1706.00428.
- [78] CMS Collaboration, “Particle-flow reconstruction and global event description with the CMS detector”, *JINST* **12** (2017) P10003, doi:10.1088/1748-0221/12/10/P10003, arXiv:1706.04965.
- [79] CMS Collaboration, “Technical proposal for the Phase-II upgrade of the Compact Muon Solenoid”, CMS Technical Proposal CERN-LHCC-2015-010, CMS-TDR-15-02, 2015.
- [80] CMS Collaboration, “Performance of electron reconstruction and selection with the CMS detector in proton-proton collisions at $\sqrt{s} = 8$ TeV”, *JINST* **10** (2015) P06005, doi:10.1088/1748-0221/10/06/P06005, arXiv:1502.02701.
- [81] CMS Collaboration, “Performance of the CMS muon detector and muon reconstruction with proton-proton collisions at $\sqrt{s} = 13$ TeV”, *JINST* **13** (2018) P06015, doi:10.1088/1748-0221/13/06/P06015, arXiv:1804.04528.
- [82] M. Cacciari, G. P. Salam, and G. Soyez, “The anti- k_T jet clustering algorithm”, *JHEP* **04** (2008) 063, doi:10.1088/1126-6708/2008/04/063, arXiv:0802.1189.
- [83] M. Cacciari, G. P. Salam, and G. Soyez, “FastJet user manual”, *Eur. Phys. J. C* **72** (2012) 1896, doi:10.1140/epjc/s10052-012-1896-2, arXiv:1111.6097.
- [84] CMS Collaboration, “Jet energy scale and resolution in the CMS experiment in pp collisions at 8 TeV”, *JINST* **12** (2017) P02014, doi:10.1088/1748-0221/12/02/P02014, arXiv:1607.03663.

-
- [85] CMS Collaboration, “Identification of heavy-flavour jets with the CMS detector in pp collisions at 13 TeV”, *JINST* **13** (2018) P05011, doi:10.1088/1748-0221/13/05/P05011, arXiv:1712.07158.
 - [86] CMS Collaboration, “Reconstruction and identification of τ lepton decays to hadrons and ν_τ at CMS”, *JINST* **11** (2016) P01019, doi:10.1088/1748-0221/11/01/P01019, arXiv:1510.07488.
 - [87] CMS Collaboration, “Performance of reconstruction and identification of τ leptons decaying to hadrons and ν_τ in pp collisions at $\sqrt{s} = 13$ TeV”, *JINST* **13** (2018) P10005, doi:10.1088/1748-0221/13/10/P10005, arXiv:1809.02816.
 - [88] CMS Collaboration, “Identification of hadronic tau lepton decays using a deep neural network”, 2022. arXiv:2201.08458. Submitted to *JINST*.
 - [89] CMS Collaboration, “Performance of missing transverse momentum in pp collisions at $\sqrt{s} = 13$ TeV using the CMS detector”, CMS Physics Analysis Summary CMS-PAS-JME-17-001, 2018.
 - [90] L. Bianchini, J. Conway, E. K. Friis, and C. Veelken, “Reconstruction of the Higgs mass in $H \rightarrow \tau\tau$ events by dynamical likelihood techniques”, *J. Phys. Conf. Ser.* **513** (2014) 022035, doi:10.1088/1742-6596/513/2/022035.
 - [91] D. Jang, “Search for MSSM Higgs decaying to τ pairs in $p\bar{p}$ collision at $\sqrt{s} = 1.96$ TeV at CDF”. PhD thesis, Rutgers U., Piscataway, 2006. doi:10.2172/892378.
 - [92] CMS Collaboration, “Observation of the Higgs boson decay to a pair of τ leptons with the CMS detector”, *Phys. Lett. B* **779** (2018) 283, doi:10.1016/j.physletb.2018.02.004, arXiv:1708.00373.
 - [93] CMS Collaboration, “An embedding technique to determine $\tau\tau$ backgrounds in proton-proton collision data”, *JINST* **14** (2019) P06032, doi:10.1088/1748-0221/14/06/p06032, arXiv:1903.01216.
 - [94] CMS Collaboration, “Measurement of the $Z\gamma^* \rightarrow \tau\tau$ cross section in pp collisions at $\sqrt{s} = 13$ TeV and validation of τ lepton analysis techniques”, *Eur. Phys. J. C* **78** (2018) 708, doi:10.1140/epjc/s10052-018-6146-9, arXiv:1801.03535.
 - [95] CMS Collaboration, “Measurement of the differential cross section for top quark pair production in pp collisions at $\sqrt{s} = 8$ TeV”, *Eur. Phys. J. C* **75** (2015) 542, doi:10.1140/epjc/s10052-015-3709-x, arXiv:1505.04480.
 - [96] CMS Collaboration, “Performance of the CMS Level-1 trigger in proton-proton collisions at $\sqrt{s} = 13$ TeV”, *JINST* **15** (2020) P10017, doi:10.1088/1748-0221/15/10/P10017, arXiv:2006.10165.
 - [97] R. Barlow and C. Beeston, “Fitting using finite Monte Carlo samples”, *Comput. Phys. Commun.* **77** (1993) 219, doi:10.1016/0010-4655(93)90005-W.
 - [98] J. S. Conway, “Incorporating nuisance parameters in likelihoods for multisource spectra”, in *PHYSTAT 2011*, p. 115. 2011. arXiv:1103.0354. doi:10.5170/CERN-2011-006.115.

- [99] G. Cowan, K. Cranmer, E. Gross, and O. Vitells, “Asymptotic formulae for likelihood-based tests of new physics”, *Eur. Phys. J. C* **71** (2011) 1554, doi:10.1140/epjc/s10052-011-1554-0, arXiv:1007.1727. [Erratum: doi:10.1140/epjc/s10052-013-2501-z].